

H α chromospheric activity of F-, G-, and K-type stars observed by the LAMOST Medium-Resolution Spectroscopic Survey

Han He^{1,2*}, Weitao Zhang³, Haotong Zhang^{1,2,4}, Song Wang^{1,2,4},
Ali Luo^{1,2,4}, Jun Zhang³

¹National Astronomical Observatories, Chinese Academy of Sciences, Beijing, 100101, China.

²University of Chinese Academy of Sciences, Beijing, 100049, China.

³School of Physics and Optoelectronics Engineering, Anhui University, Hefei, 230601, China.

⁴CAS Key Laboratory of Optical Astronomy, Chinese Academy of Sciences, Beijing, 100101, China.

*Corresponding author(s). E-mail(s): hehan@nao.cas.cn;

Abstract

The distribution of stellar **H α** chromospheric activity with respect to stellar atmospheric parameters (effective temperature T_{eff} , surface gravity $\log g$, and metallicity $[\text{Fe}/\text{H}]$) and main-sequence/giant categories is investigated for the F-, G-, and K-type stars observed by the LAMOST Medium-Resolution Spectroscopic Survey (MRS). A total of 329,294 MRS spectra from LAMOST DR8 are utilized in the analysis. The **H α** activity index ($I_{\text{H}\alpha}$) and the **H α** R -index ($R_{\text{H}\alpha}$) are evaluated for the MRS spectra. The **H α** chromospheric activity distributions with individual stellar parameters as well as in the $T_{\text{eff}} - \log g$ and $T_{\text{eff}} - [\text{Fe}/\text{H}]$ parameter spaces are analyzed based on the $R_{\text{H}\alpha}$ index data. It is found that: (1) for the main-sequence sample, the $R_{\text{H}\alpha}$ distribution with T_{eff} has a bowl-shaped lower envelope with a minimum at about 6200 K, a hill-shaped middle envelope with a maximum at about 5600 K, and an upper envelope continuing to increase from hotter to cooler stars; (2) for the giant sample, the middle and upper envelopes of the $R_{\text{H}\alpha}$ distribution first increase with a decrease of T_{eff} and then drop to a lower activity level at about 4300 K, revealing different activity characteristics at different stages of stellar evolution; (3) for both the main-sequence and giant samples, the upper envelope of the $R_{\text{H}\alpha}$ distribution with metallicity is higher for stars with $[\text{Fe}/\text{H}]$ greater than about -1.0 , and the

lowest-metallicity stars hardly exhibit high $\text{H}\alpha$ indices. A dataset of $\text{H}\alpha$ activity indices for the LAMOST MRS spectra analyzed is provided with this paper.

Keywords: Stellar activity, Stellar chromospheres, Sky surveys, Spectroscopy

1 Introduction

Stellar chromospheric magnetic activity is believed to widely exist on solar-type stars (e.g., [Hall 2008](#)). In the photosphere of stars, the magnetic activity leads to starspots and faculae, while in the chromosphere immediately above the photosphere, the magnetic activity causes bright plages which can be observed through the line core emission of the chromospheric spectral lines, such as the $\text{H}\alpha$, Ca II H and K, Ca II infrared triplet, etc. On the Sun and solar-like stars, the chromospheric emission of the $\text{H}\alpha$ line is formed at the middle height of the chromosphere ([Vernazza et al, 1981](#)); thus, the $\text{H}\alpha$ line can present abundant chromospheric features as demonstrated in the $\text{H}\alpha$ monochromatic images of the Sun (e.g., [Hale 1929](#)), and has become one of the most commonly used spectral lines for monitoring solar chromospheric activity. For stars other than the Sun, the $\text{H}\alpha$ line is also one of the important approaches to detect and diagnose the activities of stellar chromospheres (e.g., [Linsky 2017](#)), and has been included in a variety of spectroscopic observation and sky survey projects.

[Herbig \(1985\)](#) evaluated the chromospheric emission flux in the line center of $\text{H}\alpha$ line for a sample of F8–G3 main-sequence stars by subtracting a low-activity standard spectrum from the observed spectra. He found that the chromospheric emission from the $\text{H}\alpha$ line correlates linearly with the emission from the Ca II H and K lines, and the decay of the $\text{H}\alpha$ emission flux with stellar age can be fitted by a power law relation. [Pasquini and Pallavicini \(1991\)](#) calibrated the absolute chromospheric flux of $\text{H}\alpha$ line for a sample of F8–K5 main-sequence and subgiant stars. They found that the flux-flux relationship between the $\text{H}\alpha$ line and the Ca II K line of stars is similar to that of solar plages, and the $\text{H}\alpha$ flux of subgiants is typically lower than that of main-sequence stars of the same spectral type. [Lyra and Porto de Mello \(2005\)](#) followed the works of [Herbig \(1985\)](#) and [Pasquini and Pallavicini \(1991\)](#) and calibrated the chromospheric emission in $\text{H}\alpha$ line for a sample of F5–K0 solar neighborhood stars. They found a well defined age-activity relation until about 2 Gyr by using the stars of open clusters and stellar kinematic groups.

[Robinson et al \(1990\)](#) investigated the $\text{H}\alpha$ emission in stellar chromosphere for a sample of main-sequence K- and M-type stars by using the equivalent width of $\text{H}\alpha$ line as the chromospheric activity indicator. Their results confirm the presence of lower and upper limits to the $\text{H}\alpha$ equivalent width for a given spectral type of stars, and both the lower and upper limits increase toward cooler stars. [Newton et al \(2017\)](#) used the $\text{H}\alpha$ equivalent width to investigate the chromospheric activity of M-type main-sequence stars and its relation to the stellar rotation period. They found that the active and inactive M-type stars can be separated by a threshold in the mass-period parameter space, which indicates that the activity of $\text{H}\alpha$ line can be a useful approach for diagnosing rotation periods of stars. [Zhang et al \(2020b, 2021\)](#) employed

the equivalent width of H α line to analyze the variations of stellar chromospheric activity based on the H α spectral data from LAMOST Data Release 7.

The H α chromospheric activity of stars can also be indicated by the activity index of H α line, like the *S*-index introduced for the Ca II H and K lines (Wilson, 1968; Vaughan et al, 1978; Duncan et al, 1991; Baliunas et al, 1995), which is defined as the ratio of the mean flux of the H α line core emission to the mean flux of two continuum bands on the two sides of the line. Kürster et al (2003) adopted the H α activity index as the indicator of the chromospheric activity of Barnard’s star, a M4 main-sequence star that is just 1.82 pc away from the solar system. Bonfils et al (2007) used the H α activity index as one of the activity parameters to indicate the chromospheric activity of another nearby main-sequence star GJ 674 (spectral type M2.5; distance about 4.5 pc) for characterizing the exoplanet of the star. Boisse et al (2009) employed the H α activity index as one of the activity indicators to investigate the activity properties of a K-type exoplanet host star, HD 189733. Gomes da Silva et al (2011) adopted the H α activity index as one of the activity measures to investigate the long-term magnetic activities of a sample of M-type main-sequence stars from the HARPS M-dwarf planet search program. Robertson et al (2013) utilized the H α activity index to investigate the stellar cycles and mean activity levels for a sample of K5–M5 stars in solar neighborhood. They also analyzed the influence of the stellar activities revealed by the H α variation to the precision of the radial velocity measurements for the exoplanet host stars. Robertson et al (2016) used the H α activity index as one of the tracers of stellar magnetic activity to examine the activity sensitivity of eight near-infrared atomic lines for detecting exoplanets around mid- to late M stars through the radial velocity approach.

In order to compare H α activity between stars of different spectral types, a better indicator of stellar H α chromospheric activity than the H α equivalent width or the H α activity index is the ratio of the stellar H α luminosity to the stellar bolometric luminosity (e.g., Walkowicz et al 2004; West et al 2011), like the *R*-index employed for the Ca II H and K lines (e.g., Middelkoop 1982; Hartmann et al 1984; Noyes et al 1984). Walkowicz et al (2004) introduced a χ factor to help evaluate the *R*-index of H α line, which is defined as the ratio of the stellar continuum flux near H α line to the stellar bolometric flux; the *R*-index of H α line can then be obtained by multiplying the χ factor by the measured equivalent width of H α line.

The LAMOST (Large Sky Area Multi-Object Fiber Spectroscopic Telescope, also named Guoshoujing Telescope; Cui et al 2012; Zhao et al 2012) Medium-Resolution Spectroscopic Survey (MRS) has been observing the spectral data of H α line of stars since 2017. The spectral resolution power ($R = \lambda/\delta\lambda$) of the MRS data is about 7500 (Liu et al, 2020). The full wavelength range of the H α line as well as the adjacent continuum is well covered by MRS spectra. After several years of observation, the LAMOST MRS has acquired millions of spectra of celestial objects; and more than a million spectra are provided with stellar atmospheric parameters, such as effective temperature (T_{eff}), surface gravity ($\log g$), and metallicity ($[\text{Fe}/\text{H}]$). The large amount of MRS spectra is well suited for studying the overall distribution of stellar H α chromospheric activity (He et al, 2021).

In this paper, we investigate the distribution of the stellar $H\alpha$ chromospheric activity with respect to stellar atmospheric parameters and main-sequence/giant categories by using the $H\alpha$ line spectral data of MRS from LAMOST Data Release 8 (DR8). We employ the $H\alpha$ activity index and the $H\alpha$ R -index as the indicators of $H\alpha$ chromospheric activity. The spectral sample analyzed includes the MRS spectra of F-, G-, and K-type stars, in which the spectra of main-sequence stars and giants are distinguished. The $H\alpha$ chromospheric activity distributions with individual stellar parameters as well as in the $T_{\text{eff}} - \log g$ and $T_{\text{eff}} - [\text{Fe}/\text{H}]$ parameter spaces are analyzed and compared for the main-sequence and giant spectral samples .

It should be mentioned that the LAMOST Low-Resolution Spectroscopic Survey (LRS) also involves the $H\alpha$ line and can be utilized for studying the stellar $H\alpha$ chromospheric activity property (e.g., Frasca et al 2016; Zhang et al 2021). The spectral resolution power of the LRS data is about 1800 (Zhao et al 2012), which is lower than that of the MRS data. Considering that the chromospheric emission mainly comes from the narrow band at the center of the $H\alpha$ line, the MRS spectra have an advantage over the LRS spectra in resolving the line core emission. In this paper, we focus on the MRS data to investigate stellar $H\alpha$ chromospheric activity.

The content of the paper is structured as follows. In Section 2, we explain the $H\alpha$ line observations by the LAMOST MRS. In Section 3, we describe the selection procedure for the MRS spectral sample used in the analysis. In section 4, we give the specific definitions of the $H\alpha$ activity index and the $H\alpha$ R -index adopted in this work, and evaluate the values of the $H\alpha$ indices for the selected MRS spectra. In Section 5, we analyze in detail the distribution of $H\alpha$ chromospheric activity with stellar atmospheric parameters and main-sequence/giant categories based on the $H\alpha$ R -index data. In Section 6, we describe the dataset of the $H\alpha$ activity indices obtained in this work. Section 7 is the conclusion and discussion.

2 $H\alpha$ line observations by the LAMOST MRS

The MRS of LAMOST collects spectra of celestial objects in a blue band (4950–5350 Å) and a red band (6300–6800 Å) simultaneously (Liu et al, 2020). The $H\alpha$ line is included in the red band. The duration of a single exposure of MRS is about 20 minutes. An observed object is usually exposed multiple times in succession by the MRS. The coadded spectrum of the object can then be generated by combining the multiple single-exposure spectra. All the single-exposure spectra and the coadded spectrum of the observed object in one observation are stored in a same FITS data file and share a same MRS `obsid` (MRS unique observation identifier). In this work, we use the coadded spectral data of LAMOST MRS to analyze stellar $H\alpha$ chromospheric activity, for a coadded spectrum generally has a higher signal-to-noise ratio than the associated individual single-exposure spectrum.

Figure 1 gives an example of the $H\alpha$ line observations by the LAMOST MRS. The $H\alpha$ spectra in the three columns of Figure 1 (from left to right) belong to the F-, G-, and K-type main-sequence stars, respectively. In each column, the three $H\alpha$ spectra from bottom to top represent the increasing $H\alpha$ activity levels. As shown in Figure 1, LAMOST uses vacuum wavelength in the released spectral data. The vacuum

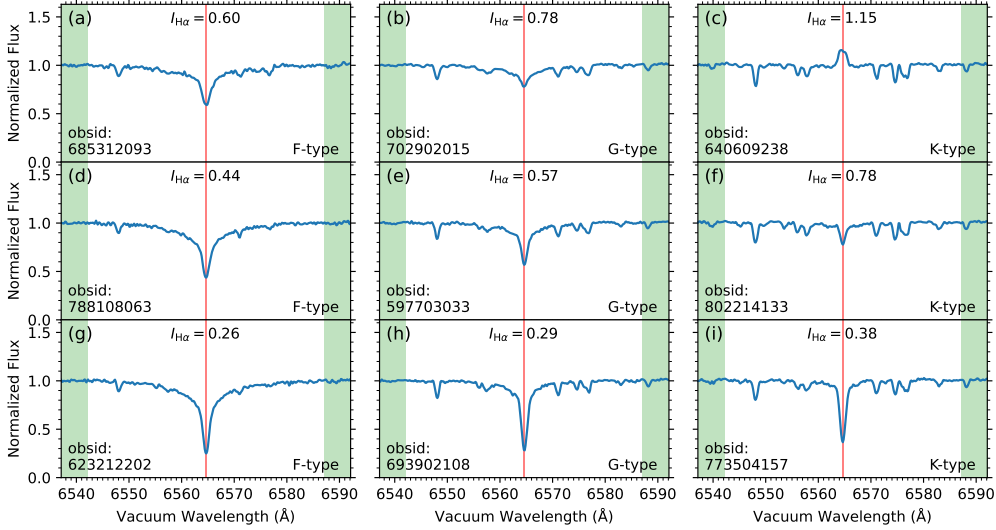


Fig. 1 Example of the $H\alpha$ line observations by the LAMOST MRS. The $H\alpha$ spectra in the three columns from left to right belong to the F-, G-, and K-type main-sequence stars, respectively. In each column, the three $H\alpha$ spectra from bottom to top represent the increasing $H\alpha$ activity levels. The wavelengths of the spectra have been transformed to the values in the rest frame. The fluxes of the spectra have been normalized by the continuum values. The center band (shown in red) and the two continuum bands (shown in green) adopted in this work for the $H\alpha$ activity index ($I_{H\alpha}$) evaluation (see Section 4.1) are indicated. The MRS *obsid* (MRS unique observation identifier) and the evaluated $I_{H\alpha}$ value are given for each of the example spectra.

wavelength of $H\alpha$ line center in the rest frame is 6564.614 \AA as adopted by the Sloan Digital Sky Survey (SDSS; [Stoughton et al 2002](#)), which can be converted to and from the air wavelength of $H\alpha$ line (6562.801 \AA) using the formula given by [Ciddor \(1996\)](#).

3 Selection of MRS spectral sample

We utilize the MRS spectra of F-, G-, and K-type stars from LAMOST DR8 v1.1¹ for the $H\alpha$ chromospheric activity analysis. The MRS data in LAMOST DR8 were observed from September 2017 to June 2020 (three full observation years). The LAMOST MRS *Parameter Catalog* of DR8 contains 1,230,307 coadded spectra of stars with determined stellar atmospheric parameters (T_{eff} , $\log g$, and $[\text{Fe}/\text{H}]$). The MRS spectral sample analyzed in this work are selected from this catalog.

The spectra of F-, G-, and K-type stars are selected from the LAMOST MRS *Parameter Catalog* by using the effective temperature condition of $4000 \text{ K} < T_{\text{eff}} < 7000 \text{ K}$ ([Johnson, 1966](#)). We use the effective temperature parameter `teff_lasp` included in the catalog (and the parameters `logg_lasp` and `feh_lasp` for the surface gravity and metallicity, respectively, in the following analysis) to perform the spectral sample selection, which is provided by the LAMOST Stellar Parameter Pipeline

¹<http://www.lamost.org/dr8/v1.1/>

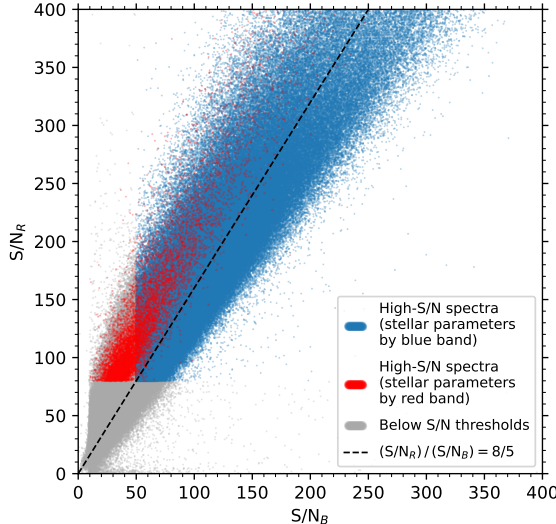


Fig. 2 Scatter diagram of S/N_B versus S/N_R for the MRS spectra of F-, G-, and K-type stars ($4000 \text{ K} < T_{\text{eff}} < 7000 \text{ K}$) in the LAMOST MRS Parameter Catalog. The dashed line indicates the ratio of $(S/N_R)/(S/N_B) = 8/5$. The high-S/N spectra that meet the S/N conditions (see main text for details) are highlighted in blue and red for the samples whose stellar atmospheric parameters are determined by the blue band and red band of MRS, respectively. The spectral sample below the S/N thresholds is displayed in gray. Note that the maximum S/N value of the MRS spectra is 1000; the range of the axes is limited to 400 to better illustrate the S/N thresholds for selection of the high-S/N spectra.

(LASP; Luo et al 2015). The number of the MRS spectra in the catalog that meet the above T_{eff} condition is 1,148,919.

LAMOST provides separate signal-to-noise ratio (S/N) parameters for the blue and red bands of MRS (denoted by S/N_B and S/N_R , respectively), which are the median of the S/N values of all data points in a band. We select the spectra with high S/N values for our analysis, as a higher S/N generally corresponds to a smaller uncertainty of spectral fluxes and more accurate stellar atmospheric parameters determined from the spectra (Luo et al, 2015). In Figure 2, we show a scatter diagram of S/N_B versus S/N_R ² for the spectra of F-, G-, and K-type stars in the LAMOST MRS Parameter Catalog to illustrate the selection of the high-S/N spectra.

Since the $H\alpha$ line is in the red band of MRS, to select the high-S/N spectra, we first introduce an S/N condition of $S/N_R \geq 80.0$ for the red band data of MRS. The threshold of S/N_R is determined empirically to ensure an appropriate upper limit of the uncertainties of the evaluated $H\alpha$ activity index values (see Section 4.1). On the other hand, there are only a small fraction of the MRS spectra whose stellar atmospheric parameters are determined by the red band of MRS, and the stellar parameters of most MRS spectra are determined based on the blue band of MRS (see the data release documents of LAMOST for more details). For the spectra whose stellar parameters are determined by the blue band, in addition to the red band S/N condition, we introduce

²The values of S/N_B and S/N_R are from the LAMOST MRS General Catalog.

another S/N condition for the blue band data of MRS, which is $S/N_B \geq 50.0$. The threshold of S/N_B is determined from the S/N_R threshold by considering that, for the MRS spectra of F-, G-, and K-type stars, the ratio of $(S/N_R)/(S/N_B)$ is roughly 8/5 as demonstrated in Figure 2.

From the LAMOST MRS Parameter Catalog, we find 417,935 MRS spectra of F-, G-, and K-type stars that meet the above S/N conditions, in which the stellar parameters of 408,309 spectra are determined by the blue band of MRS, and the stellar parameters of 9,626 spectra are determined by the red band of MRS. The two sets of samples are highlighted in blue and red, respectively, in Figure 2.

LAMOST MRS Parameter Catalog also provides the projected rotational velocity ($v\sin i$) values determined by the LAMP (parameter `vsini_lasp` in the catalog) for the spectra with $v\sin i > 30$ km/s. The rotational broadening of H α line caused by a large $v\sin i$ can affect the evaluated values of the H α activity index (see Section 4.1 and Appendix B). To minimize the effects of rotational broadening, we only keep the spectra with $v\sin i$ less than 30 km/s, i.e., the spectra whose `vsini_lasp` values are not available in the catalog (indicated by a value of -9999.0). The number of the selected spectra after this condition is 337,742. Those spectra with $v\sin i$ greater than 30 km/s (80,193 in total) are removed from our sample.

Some of the MRS spectra have invalid flux values in the wavelength range of H α line (e.g., flux equaling to or less than zero) or missing auxiliary parameters in the LAMOST MRS catalog (e.g., the parameter of radial velocity used in Section 4.1); a small portion of the MRS spectra comes from the stellar objects close to or in the Galactic nebulae, which belong to the LAMOST medium-resolution spectral survey of Galactic Nebulae (MRS-N), a sub-project of LAMOST MRS (see Wu et al 2021, 2022a for more details). These spectra are also removed from our sample. We finally get 329,294 MRS spectra of F-, G-, and K-type stars for the following H α chromospheric activity analysis.

Because the main-sequence and giant stars are at different evolution stages and might present different chromospheric activity properties (e.g., Pasquini and Pallavicini 1991; Lyra and Porto de Mello 2005), we distinguish the two stellar categories in the analysis. To illustrate the partitioning of the main-sequence and giant samples, in Figure 3 we show the distribution of the selected MRS spectra of F-, G-, and K-type stars in the $T_{\text{eff}} - \log g$ parameter space, with number density of the spectral sample being indicated by color scale. The horizontal and vertical lines in Figure 3 are the dividing lines for the main-sequence and giant samples, whose position is determined by referring to the stellar parameter ranges of main-sequence and giant stars in the literature (e.g., Straižys and Kuriliene 1981; Buder et al 2019; García and Ballot 2019; Kiefer et al 2019; Zhang et al 2020b; Chen et al 2022). As shown in Figure 3, we use the condition of $\log g \geq 3.9$ for the main-sequence sample (bottom region in Figure 3), and the condition of $T_{\text{eff}} < 5400$ K and $\log g < 3.8$ for the giant sample (upper-right region in Figure 3). The main-sequence and giant regions are separated by an intermediate zone to ensure the purity of the two samples. In the selected MRS spectra of F-, G-, and K-type stars, the numbers of the main-sequence spectra and the giant spectra that meet the above conditions are 188,617 and 121,740,

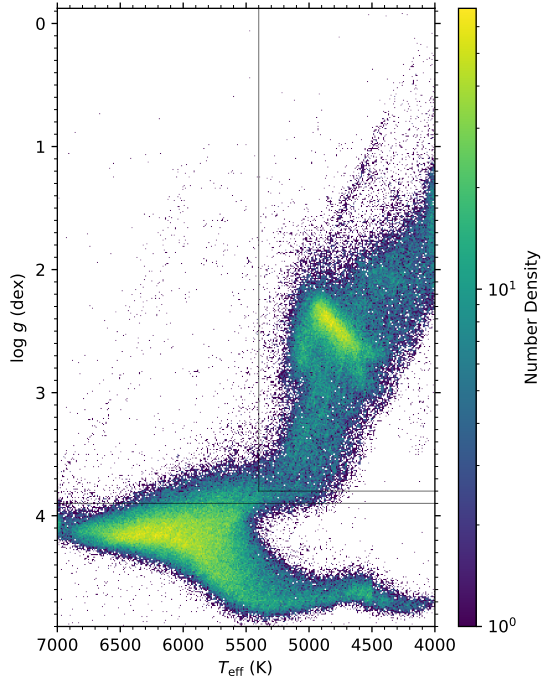


Fig. 3 Distribution of the selected MRS spectra of F-, G-, and K-type stars in the $T_{\text{eff}} - \log g$ parameter space. Color scale indicates number density of the spectral sample. The horizontal and vertical lines (corresponding to $\log g = 3.9$, $\log g = 3.8$, and $T_{\text{eff}} = 5400$ K, respectively, from bottom to top) are the dividing lines for the main-sequence sample (bottom region) and the giant sample (upper-right region).

respectively. Although not included in the main-sequence or giant sample, the spectra in the intermediate zone (18,937 in total) are still used in the analysis.

Because the stellar atmospheric parameters determined by the LAMP (`teff_lasp`, `logg_lasp`, and `feh_lasp` in the LAMOST MRS Parameter Catalog) are extensively used in our analysis, to rule out the possibility of degeneracy between the stellar parameter values, we examine the distribution of the $[\text{Fe}/\text{H}]$ values in the $T_{\text{eff}} - \log g$ parameter space for the selected MRS spectra of F-, G-, and K-type stars (see Appendix A for details). The result does not suggest a degeneracy (apparent correlation) between the values of $[\text{Fe}/\text{H}]$ and the values of T_{eff} (or $\log g$), which demonstrates the reliability of the stellar atmospheric parameter values.

4 $\text{H}\alpha$ indices of stellar chromospheric activity

4.1 $\text{H}\alpha$ activity index

We employ the $\text{H}\alpha$ activity index (denoted by $I_{\text{H}\alpha}$) as the primary index of stellar $\text{H}\alpha$ chromospheric activity, for it directly relies on the observed spectral flux data of MRS. The $\text{H}\alpha$ activity index is defined as the ratio of the mean flux of the center band

of H α line to the mean flux of two continuum bands on the two side of H α line, i.e. (e.g., Kürster et al 2003; Robertson et al 2013),

$$I_{\text{H}\alpha} = \frac{\overline{F}_{\text{H}\alpha}}{\overline{F}_{\text{cont}}} = \frac{\overline{F}_{\text{H}\alpha}}{(\overline{F}_{\text{cont},1} + \overline{F}_{\text{cont},2})/2}, \quad (1)$$

where F represents the observed flux data of MRS, $\overline{F}_{\text{H}\alpha}$ is the mean flux of the H α center band, $\overline{F}_{\text{cont},1}$ and $\overline{F}_{\text{cont},2}$ are the mean fluxes of the continuum bands on the blue side and red side of H α line, respectively, and $\overline{F}_{\text{cont}} = (\overline{F}_{\text{cont},1} + \overline{F}_{\text{cont},2})/2$ is the mean flux of the both continuum bands. The value of $I_{\text{H}\alpha}$ defined by Equation (1) is in the range of 0.0–1.0 for the H α absorption line profile and greater than 1.0 for the H α emission line profile (see example in Figure 1).

To evaluate the H α activity index based on Equation (1), Kürster et al (2003), Bonfils et al (2007), and Boisse et al (2009) adopted a center bandwidth of H α line of 0.678 Å, while Gomes da Silva et al (2011) and Robertson et al (2013, 2016) used a 1.6 Å wide center band. The two continuum bands chosen by these works are centered at 6550.87 Å and 6580.31 Å (wavelengths in air) with bandwidths of 10.75 Å and 8.75 Å, respectively (Kürster et al 2003; Gomes da Silva et al 2011), which are optimized and hence more suitable for the relatively narrow H α line profiles of K- and M-type stars.

In this work, we extend the H α activity index analysis to F- and G-type stars. To match the relatively wider H α line profiles of these types of stars as demonstrated in Figure 1, we adopt a different definition of the center and continuum bands of H α line than that for the K- and M-type stars described above. In our definition, the width of the center band of H α line is set to 0.25 Å, which is commonly used by the solar H α filtergram observations (e.g., Zhang et al 2007; Fang et al 2013; Liu et al 2014; Ichimoto et al 2017) to minimize the contamination of photospheric radiation from the line wings. The center wavelengths of the two continuum bands are both 25 Å away from the line center of H α line, and the width of each continuum band is set to 5 Å. A diagram illustration of the center and continuum bands adopted in this work for the $I_{\text{H}\alpha}$ evaluation has been given in Figure 1.

Owing to the radial velocities of the observed stellar objects, the wavelength values in the original MRS spectral data need to be transformed to the wavelengths in the rest frame before $I_{\text{H}\alpha}$ evaluation. We adopt the radial velocity parameter `rv_r0` included in the LAMOST MRS Parameter Catalog to perform the wavelength transformation, which is determined based on the red band spectra of MRS by cross-correlation with the template spectra (see the data release documents of LAMOST for more details).

We calculate the values of $I_{\text{H}\alpha}$ using Equation (1) for all the MRS spectra of F-, G-, and K-type stars selected in Section 3. The stochastic uncertainties of the $I_{\text{H}\alpha}$ values (denoted by $\delta I_{\text{H}\alpha}$) are also estimated, which takes into account the spectral flux uncertainty, the radial velocity uncertainty, and the discretization in the spectral data (Zhang et al 2022). Figure 4 shows the histograms of the evaluated $I_{\text{H}\alpha}$ index values and the estimated uncertainties of $I_{\text{H}\alpha}$. It can be seen from Figure 4 that most $I_{\text{H}\alpha}$ values are distributed in the range of less than about 1.7, and the uncertainties of $I_{\text{H}\alpha}$ are on the order of magnitude of 10^{-3} to 10^{-2} . The data of the obtained $I_{\text{H}\alpha}$

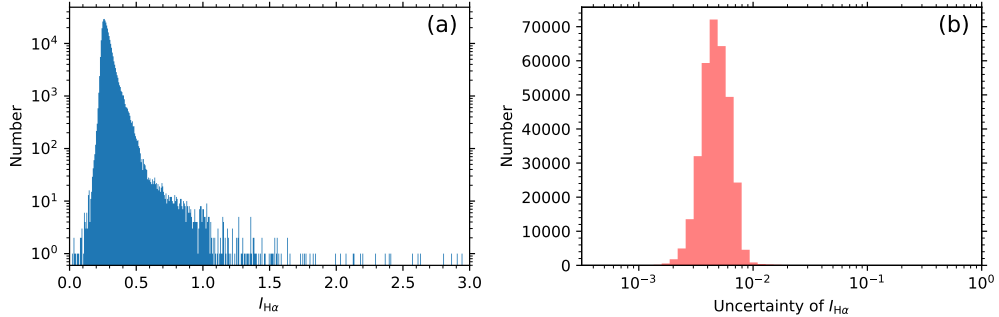


Fig. 4 Histograms of the evaluated $I_{H\alpha}$ index values (panel a) and their uncertainties (panel b) for the selected MRS spectra of F-, G-, and K-type stars.

index values and their uncertainties are available in the online dataset of this paper (see Section 6).

It needs to be noted that the projected rotational velocity, $v \sin i$, can distort the shape of the $H\alpha$ line owing to the rotational broadening effect (e.g., Herbig 1985; Pasquini and Pallavicini 1991), and hence leads to an increment of $I_{H\alpha}$ values (denoted by $\Delta I_{H\alpha}$) which takes a positive value for the absorption line profile and negative value for the emission line profile. For this reason, we have removed the spectra with $v \sin i$ greater than 30 km/s from our sample, as described in Section 3. LAMOST MRS catalog does not provide $v \sin i$ values for the spectra with $v \sin i$ less than 30 km/s, therefore, 30 km/s can be regarded as the upper limit of $v \sin i$ for the MRS spectral sample analyzed in this work.

In Appendix B, we estimate the relationship between the magnitudes of $v \sin i$ and $\Delta I_{H\alpha}$ by using the nine example spectra shown in Figure 1. The results are plotted in Figure B2. It can be seen from Figure B2 that for the $v \sin i$ values less than 30 km/s, the absolute magnitude of $\Delta I_{H\alpha}$ is generally below about $0.02 \sim 0.05$ for higher $I_{H\alpha}$ values (panels a–f of Figure B2) and below about $0.06 \sim 0.08$ for lower $I_{H\alpha}$ values (panels g–i of Figure B2). The spectra with a lower $I_{H\alpha}$ tend to have a larger $\Delta I_{H\alpha}$ owing to their deeper spectral line profile (see panels g–i of Figure 1). On the other hand, stars with a lower level of activity generally have a smaller value of rotational velocity according to the activity–rotation relationship of stars (e.g., Noyes et al 1984; Wright et al 2011; Astudillo-Defru et al 2017; Newton et al 2017; Wang et al 2020; Han et al 2023), which can effectively mitigate the large $\Delta I_{H\alpha}$ in panels g–i of Figure B2. If $v \sin i$ is less than 20 km/s, the magnitude of $\Delta I_{H\alpha}$ in panels g–i of Figure B2 would be below 0.05. Putting the above discussions together, for the MRS spectral sample analyzed in this work, the absolute magnitude of $\Delta I_{H\alpha}$ as a whole can be considered to be generally less than about 0.05, which is on the same order of magnitude as the stochastic uncertainty of $I_{H\alpha}$.

4.2 H α R -index

The values of the $I_{\text{H}\alpha}$ index obtained in Section 4.1 are affected by the continuum flux which in turn is a function of stellar atmospheric parameters. For that reason, we employ the H α R -index (denoted by $R_{\text{H}\alpha}$) as the secondary index of stellar H α chromospheric activity, which is defined as the ratio of the stellar H α luminosity to the stellar bolometric luminosity (e.g, Walkowicz et al 2004; West et al 2011), i.e.,

$$R_{\text{H}\alpha} = \frac{L_{\text{H}\alpha}}{L_{\text{bol}}} = \frac{\mathcal{F}_{\text{H}\alpha}}{\mathcal{F}_{\text{bol}}}, \quad (2)$$

where L represents the stellar luminosity and \mathcal{F} represents the flux density (energy per unit time per unit area) on the stellar surface. Note that $L = \mathcal{F} \cdot A_*$, where A_* is the stellar surface area.

The $R_{\text{H}\alpha}$ index defined in Equation (2) eliminates the effect of continuum flux variation, and therefore is more suitable for comparing the activity properties of different types of stars.

The \mathcal{F}_{bol} in Equation (2) can be expressed by T_{eff} as

$$\mathcal{F}_{\text{bol}} = \sigma T_{\text{eff}}^4, \quad (3)$$

where σ is the Stefan-Boltzmann constant. The $\mathcal{F}_{\text{H}\alpha}$ in Equation (2) can be expressed as

$$\mathcal{F}_{\text{H}\alpha} = \Delta\lambda \cdot \bar{f}_{\text{H}\alpha} = \Delta\lambda \cdot \bar{f}_{\text{cont}} \cdot \frac{\bar{f}_{\text{H}\alpha}}{\bar{f}_{\text{cont}}} = \Delta\lambda \cdot \bar{f}_{\text{cont}} \cdot \frac{\bar{F}_{\text{H}\alpha}}{\bar{F}_{\text{cont}}} = \Delta\lambda \cdot \bar{f}_{\text{cont}} \cdot I_{\text{H}\alpha}, \quad (4)$$

where $\Delta\lambda$ is the width of the center band of H α line (equaling to 0.25 Å as defined in Section 4.1), f represents the spectral flux density (energy per unit time per unit area per unit wavelength) on the stellar surface, $\bar{f}_{\text{H}\alpha}$ is the mean value of f in the center band of H α line, \bar{f}_{cont} is the mean value of f in the two continuum bands defined in Section 4.1, and F represents the observed flux data of MRS which is the same as in Equation (1).

By substituting Equations (3) and (4) into Equation (2), we obtain

$$R_{\text{H}\alpha} = \Delta\lambda \cdot \frac{\bar{f}_{\text{cont}}}{\sigma T_{\text{eff}}^4} \cdot I_{\text{H}\alpha} = \Delta\lambda \cdot \chi \cdot I_{\text{H}\alpha}, \quad (5)$$

where the factor

$$\chi = \bar{f}_{\text{cont}} / (\sigma T_{\text{eff}}^4) \quad (6)$$

which is a function of stellar atmospheric parameters (Walkowicz et al, 2004) and in unit of Å⁻¹.

To evaluate the value of $R_{\text{H}\alpha}$ from $I_{\text{H}\alpha}$ using Equation (5), one should first know the value of the factor χ . In this work, we obtain the χ values by using the library of synthetic spectra of stellar atmospheres presented in Husser et al (2013), which is based on the PHOENIX stellar atmospheric code (Allard and Hauschildt, 1995; Allard,

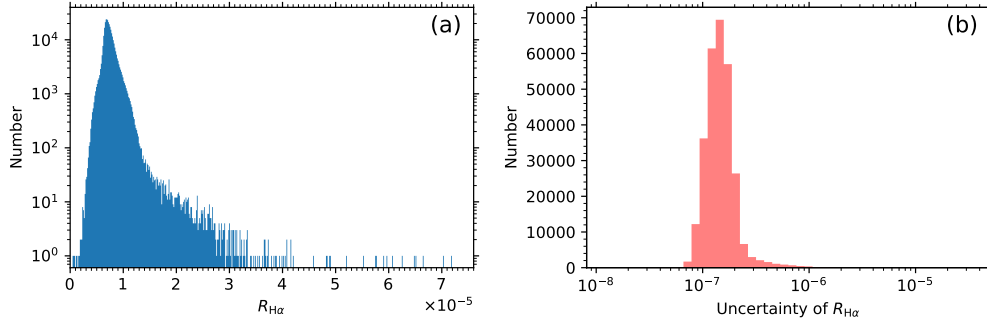


Fig. 5 Histograms of the evaluated $R_{H\alpha}$ index values (panel a) and their uncertainties (panel b) for the selected MRS spectra of F-, G-, and K-type stars.

2016). The synthetic spectra of stellar atmospheres provide the data of f with physical units, thus the χ values can be calculated directly from the synthetic spectra by using Equation (6). A comparison by Lançon et al (2021) between the synthetic spectra of Husser et al (2013) and the observed spectra across the Hertzsprung-Russell diagram showed that a satisfactory representation of the continuum flux can be obtained by the synthetic spectra in the visual band with stellar effective temperature down to about 4000 K (see Lançon et al 2021 for details). The library of stellar synthetic spectra by Husser et al (2013) only provides the spectral data of a grid of stellar atmospheric parameters; for the stellar parameters between the grid points, the value of χ is obtained via interpolation based on the χ values on the grid. The uncertainties of the obtained χ values (denoted by $\delta\chi$) depend on the uncertainties of the stellar atmospheric parameters (δT_{eff} , $\delta \log g$, and $\delta[\text{Fe}/\text{H}]$) of the MRS spectra, and the latter has been provided by the LAMOST MRS Parameter Catalog. The algorithm for the $\delta\chi$ estimation is described in Appendix C.

We calculate the values of $R_{H\alpha}$ using Equation (5) for the selected MRS spectra of F-, G-, and K-type stars. The stochastic uncertainties of the $R_{H\alpha}$ values (denoted by $\delta R_{H\alpha}$) are estimated from $\delta\chi$ and $\delta I_{H\alpha}$ using the error propagation rules. Five MRS spectra in the giant sample have $\log g$ values less than zero, which are out of the parameter scope of the synthetic spectra by Husser et al (2013); so the χ and $R_{H\alpha}$ values of the five MRS spectra are not calculated. In addition to the five spectra, the δT_{eff} , $\delta \log g$, and $\delta[\text{Fe}/\text{H}]$ values of a few MRS spectra are not fully available in the LAMOST catalog, and the values of $\log g - \delta \log g$ of very few spectra are out of the parameter scope of the synthetic spectra; for these spectra (47,495 in total), the uncertainties of χ , and hence the uncertainties of $R_{H\alpha}$, are not estimated.

Figure 5 shows the histograms of the evaluated $R_{H\alpha}$ index values and the estimated uncertainties of $R_{H\alpha}$. It can be seen from Figure 5 that the $R_{H\alpha}$ values are on the order of magnitude of 10^{-5} , and the uncertainties of $R_{H\alpha}$ are on the order of magnitude of 10^{-7} . All data of the obtained $R_{H\alpha}$ index values and their uncertainties, as well as the associated χ values and their uncertainties, are available in the online dataset of this paper (see Section 6). The missing values of $R_{H\alpha}$, $\delta R_{H\alpha}$, χ , and $\delta\chi$ mentioned above are indicated by -9999.0 in the dataset.

5 Distribution of the H α chromospheric activity

By using the $R_{\text{H}\alpha}$ index values obtained in Section 4 for the selected MRS spectral sample of F-, G-, and K-type stars, we analyze in detail the distribution of H α chromospheric activity with respect to stellar atmospheric parameters and main-sequence/giant categories. In Section 5.1, we analyze and compare the $R_{\text{H}\alpha}$ index distributions with individual stellar atmospheric parameters (T_{eff} , $\log g$, and [Fe/H]) for the main-sequence and giant samples. In Sections 5.2 and 5.3, we further investigate the distributions of the $R_{\text{H}\alpha}$ index values in the $T_{\text{eff}} - \log g$ and $T_{\text{eff}} - [\text{Fe}/\text{H}]$ parameter spaces, respectively.

5.1 Distribution of the $R_{\text{H}\alpha}$ index with T_{eff} , $\log g$, and [Fe/H] for the main-sequence and giant samples

Figure 6 shows the distribution of the $R_{\text{H}\alpha}$ index values with effective temperature T_{eff} (left column), surface gravity $\log g$ (middle column), and metallicity [Fe/H] (right column) for the selected MRS spectra of main-sequence sample (top row), giant sample (middle row), and both categories (bottom row).

The distributions of $R_{\text{H}\alpha}$ with T_{eff} for the main-sequence and giant samples are distinctly different as exhibited in the left column (panels a, d, and g) of Figure 6.

As shown in Figure 6a, there are three apparent envelopes in the $R_{\text{H}\alpha}$ versus T_{eff} distribution plot of the main-sequence sample: a bowl-shaped lower envelope, a hill-shaped middle envelope, and an upper envelope continuing to increase from hotter to cooler stars. These envelopes are characterized by a sharp change in the number density of spectral sample. The lower envelope in Figure 6a has a minimum $R_{\text{H}\alpha}$ value of about 0.55×10^{-5} at about 6200 K, and the middle envelope has a maximum $R_{\text{H}\alpha}$ value of about 1.55×10^{-5} at about 5600 K. The distinction between the upper envelope and the middle envelope in Figure 6a is most pronounced in the T_{eff} range cooler than 6000 K, and the $R_{\text{H}\alpha}$ values of the upper envelope continue to increase from the middle envelope value at about 6000 K to about 3.70×10^{-5} at 4000 K.

For the giant sample, the $R_{\text{H}\alpha}$ versus T_{eff} distribution plot (see Figure 6d) also presents the lower, middle, and upper envelopes. However, the lower envelope of the giant sample in Figure 6d continues to decrease from hotter to cooler stars, and both the middle and upper envelopes first increase with decrease of T_{eff} and then drop to a lower activity level at about 4300 K. The middle envelope in Figure 6d reaches a maximum $R_{\text{H}\alpha}$ value of about 1.55×10^{-5} at about 4550 K, and the upper envelope reaches a maximum $R_{\text{H}\alpha}$ value of about 2.70×10^{-5} at about 4800 K. These features in $R_{\text{H}\alpha}$ versus T_{eff} distribution plot of the giant sample are distinctly different from those of the main-sequence sample, revealing the different activity characteristics at different stages of stellar evolution.

The middle column of Figure 6 (panels b, e, and h) shows the distributions of $R_{\text{H}\alpha}$ with $\log g$ for the main-sequence and giant samples. The distribution plot in Figure 6h ($R_{\text{H}\alpha}$ versus $\log g$ for both the main-sequence and giant samples) suggests that a larger surface gravity favors a higher $R_{\text{H}\alpha}$ index, but the shape of the envelopes in the plot is complicated and the trend is not monotonic.

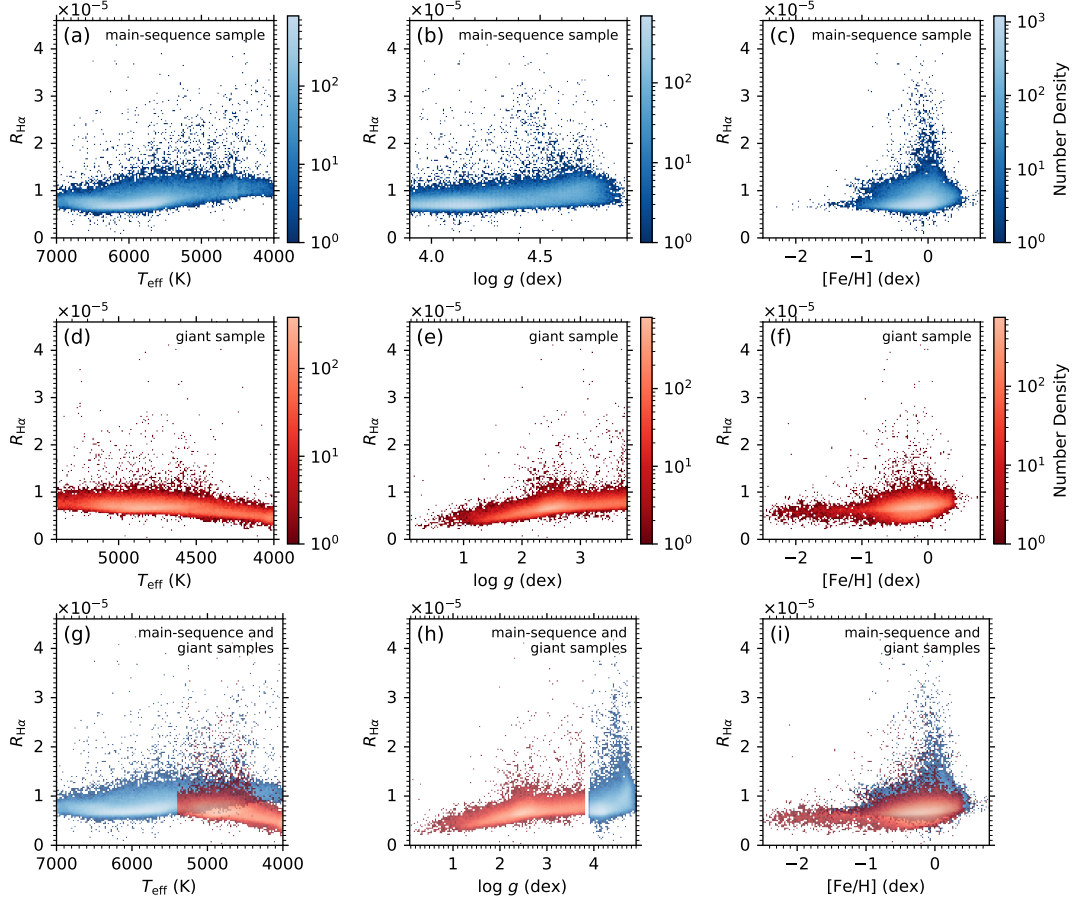


Fig. 6 Distribution of the $R_{\text{H}\alpha}$ index values with T_{eff} (left column), $\log g$ (middle column), and $[\text{Fe}/\text{H}]$ (right column) for the selected MRS spectra of main-sequence sample (top row), giant sample (middle row), and both categories (bottom row). Color scale indicates number density of the spectral sample (main-sequence sample in blue and giant sample in red).

From the right column of Figure 6 (panels c, f, and i) it can be seen that the distributions of $R_{\text{H}\alpha}$ with $[\text{Fe}/\text{H}]$ for the main-sequence and giant samples are similar in the sense that the upper envelopes in the $R_{\text{H}\alpha}$ versus $[\text{Fe}/\text{H}]$ distribution plots are higher for stars with $[\text{Fe}/\text{H}]$ greater than about -1.0 , and the metal-poor stars with $[\text{Fe}/\text{H}]$ less than about -1.0 generally have a lower level of $\text{H}\alpha$ activity. The fact that the lowest-metallicity stars hardly exhibit high $\text{H}\alpha$ indices implies that they might be very old stars (e.g., Soderblom 2010; Frebel and Norris 2015).

The bottom row of Figure 6 (panels g, h, and i) displays the distributions of $R_{\text{H}\alpha}$ with the three stellar atmospheric parameters for both the main-sequence and giant samples (main-sequence sample in blue and giant sample in red) so that the $R_{\text{H}\alpha}$ index distributions of the two stellar categories can be compared directly. The distribution

plots of $R_{\text{H}\alpha}$ versus the three stellar parameters all exhibit that the H α chromospheric activity of giant stars is on average lower than that of main-sequence stars, which is consistent with the results in the literature (e.g., Pasquini and Pallavicini 1991; Lyra and Porto de Mello 2005).

It needs to be mentioned that some spectra have isolated ultra-high $R_{\text{H}\alpha}$ values relative to the upper envelope of the $R_{\text{H}\alpha}$ distributions as displayed in Figure 6. These ultra-high values of H α indices can also be seen in the histogram of $R_{\text{H}\alpha}$ in Figure 5a as well as in the histogram of $I_{\text{H}\alpha}$ in Figure 4a. Most of the ultra-high values of H α indices come from the transient eruption events (such as stellar flares) as indicated by the associated MRS single-exposure spectra, which show rapid time-sequence evolution of H α line profiles within a couple of hours (e.g., Wu et al 2022b; Lu et al 2022). In this work, we focus on the stellar chromospheric activity in the usual sense, i.e., the activity associated with the steady state of stellar chromosphere (Hall 2008). The spectra of the transient eruption events will be studied in the future research.

We also examine those few data points beneath the lower envelope of the $R_{\text{H}\alpha}$ distributions shown in Figure 6. Most of the data points are associated with abnormal spectral profiles in original MRS spectral data and can therefore be regarded as outliers.

5.2 Distribution of the $R_{\text{H}\alpha}$ index in the $T_{\text{eff}} - \log g$ parameter space

To investigate the connections between the $R_{\text{H}\alpha}$ index distributions with respect to individual stellar atmospheric parameters presented in Section 5.1, in this subsection we further analyze the distribution of the $R_{\text{H}\alpha}$ values in the $T_{\text{eff}} - \log g$ parameter space, and the $R_{\text{H}\alpha}$ distribution in the $T_{\text{eff}} - [\text{Fe}/\text{H}]$ parameter space will be analyzed in Section 5.3.

Figure 7a shows the distribution of the $R_{\text{H}\alpha}$ index values in the $T_{\text{eff}} - \log g$ parameter space for the selected MRS spectra of F-, G-, and K-type stars. The value of $R_{\text{H}\alpha}$ is indicated by color scale. The data points in Figure 7a are stacked in ascending order of their $R_{\text{H}\alpha}$ values, with the maximum value at the highest layer and the minimum value at the lowest layer. The horizontal and vertical lines in Figure 7a are the dividing lines for the main-sequence and giant samples (same as in Figure 3). For comparison with the results in Section 5.1, we also show the scatter plots of $R_{\text{H}\alpha}$ versus T_{eff} for the giant sample and the main-sequence sample in Figures 7b and 7c, respectively, with the same $R_{\text{H}\alpha}$ color scale as in Figure 7a.

As demonstrated in Figure 7, the magnitude of $R_{\text{H}\alpha}$ can be roughly divided into three levels: the lower level ($R_{\text{H}\alpha}$ less than about 1.05×10^{-5}), the middle level ($R_{\text{H}\alpha}$ between about 1.05×10^{-5} and 1.55×10^{-5}), and the upper level ($R_{\text{H}\alpha}$ greater than about 1.55×10^{-5}), which are displayed in blue, green, and red, respectively, in Figure 7. The three levels of $R_{\text{H}\alpha}$ values are also distinguished by two horizontal lines (representing $R_{\text{H}\alpha} = 1.05 \times 10^{-5}$ and 1.55×10^{-5} , respectively) in Figures 7b and 7c. It can be seen from Figures 7b and 7c that the lower, middle, and upper envelopes in the $R_{\text{H}\alpha}$ versus T_{eff} distribution plots discussed in Section 5.1 are roughly associated with the lower, middle, and upper levels of $R_{\text{H}\alpha}$ values, respectively.

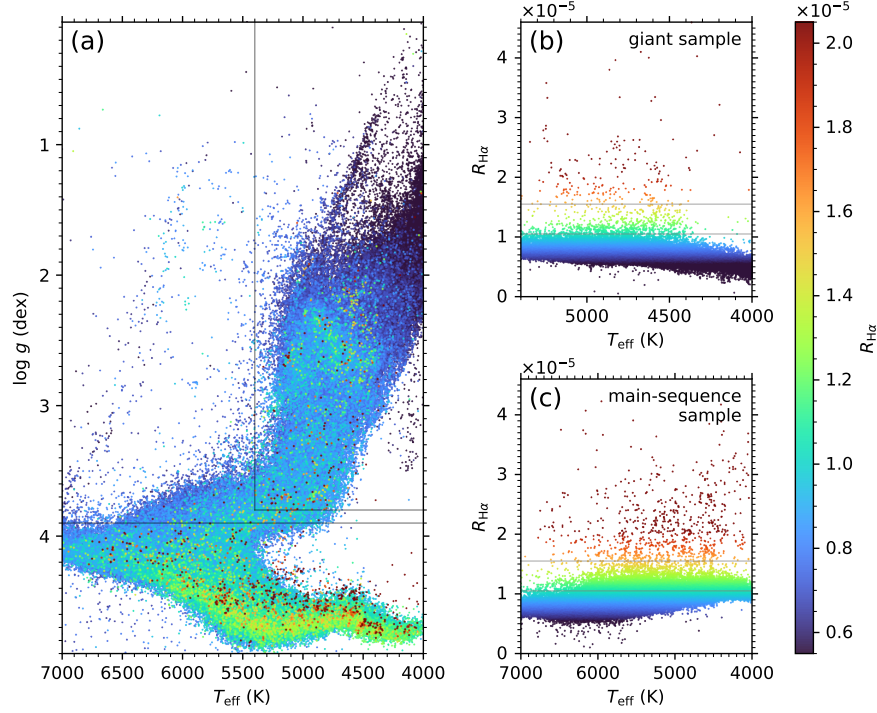


Fig. 7 (a) Distribution of the $R_{H\alpha}$ index values in the $T_{\text{eff}} - \log g$ parameter space for the selected MRS spectra of F-, G-, and K-type stars. The value of $R_{H\alpha}$ is indicated by color scale. The data points in the diagram are stacked in ascending order of their $R_{H\alpha}$ values, with the maximum value at the highest layer and the minimum value at the lowest layer. The horizontal and vertical lines in the diagram are the dividing lines for the main-sequence and giant samples (same as in Figure 3). (b) Scatter plot of $R_{H\alpha}$ versus T_{eff} for the giant sample. (c) Scatter plot of $R_{H\alpha}$ versus T_{eff} for the main-sequence sample. Panels b and c use the same $R_{H\alpha}$ color scale as panel a. The two horizontal lines in panels b and c represent $R_{H\alpha} = 1.05 \times 10^{-5}$ and 1.55×10^{-5} , respectively, for distinguishing the three levels of $R_{H\alpha}$ values (see main text for details).

The distribution areas of the three levels of $R_{H\alpha}$ values in the $T_{\text{eff}} - \log g$ parameter space are different as exhibited in Figure 7a. The lower-level $R_{H\alpha}$ values (displayed in blue) occupy the largest area in the $T_{\text{eff}} - \log g$ space and encompass the vast majority of the spectral sample. The distribution area of the middle-level $R_{H\alpha}$ values (displayed in green) is less than that of the of the lower-level $R_{H\alpha}$ values. For the main-sequence sample, most of the middle-level $R_{H\alpha}$ values distribute along the usual main-sequence strip zone in the $T_{\text{eff}} - \log g$ space; while for the giant sample, the middle-level $R_{H\alpha}$ values spread over an irregularly shaped area. The upper-level $R_{H\alpha}$ values (displayed in red) occupy the smallest area in the $T_{\text{eff}} - \log g$ space, and the location of the upper-level $R_{H\alpha}$ values in the $T_{\text{eff}} - \log g$ space does not exactly coincide with that of the middle-level $R_{H\alpha}$ values for both the main-sequence and giant samples. For the main-sequence sample, the difference between the locations of the middle-level and upper-level $R_{H\alpha}$ values in the $T_{\text{eff}} - \log g$ space suggests that they might be associated

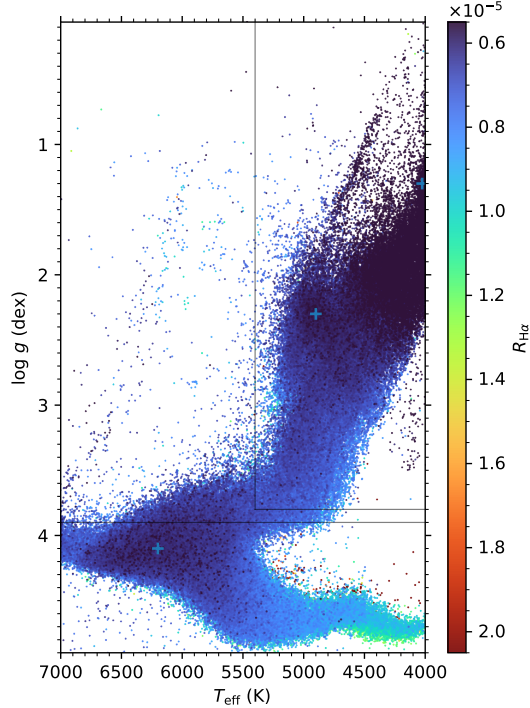


Fig. 8 Distribution of the bottommost $R_{H\alpha}$ index values in the $T_{\text{eff}} - \log g$ parameter space for the selected MRS spectra of F-, G-, and K- type stars. The value of $R_{H\alpha}$ is indicated by color scale (same as in Figure 7, but with an inverted $R_{H\alpha}$ -axis of colorbar). The data points in the diagram are stacked in reverse order of their $R_{H\alpha}$ values, with the minimum value at the highest layer and the maximum value at the lowest layer. The horizontal and vertical lines in the diagram are the dividing lines for the main-sequence and giant samples (same as in Figure 3). The ‘+’ symbol indicates the local areas with the minimum $R_{H\alpha}$ values (displayed in deep blue; see main text for details).

with stars at different evolution stages and ages (e.g., [Pecaut and Mamajek 2013](#); [Baraffe et al 2015](#)), that is, the younger the star, the higher the activity level.

In Figure 7a, the bottommost data points of the $R_{H\alpha}$ values are obscured by the higher data points and hence are not visible. In Figure 8 we show the dedicated diagram of the $R_{H\alpha}$ index distribution in the $T_{\text{eff}} - \log g$ parameter space for the bottommost $R_{H\alpha}$ values. The color scale of $R_{H\alpha}$ in Figure 8 is the same as in Figure 7, but the data points are stacked in reverse order of their $R_{H\alpha}$ values, i.e., the minimum value at the highest layer and the maximum value at the lowest layer.

As shown in Figures 7b and 7c, the minimum $R_{H\alpha}$ values (displayed in deep blue) are around 0.55×10^{-5} for the main-sequence sample and less than about 0.60×10^{-5} for the giant sample. These minimum $R_{H\alpha}$ values are distributed in separate deep blue areas in the $T_{\text{eff}} - \log g$ parameter space as demonstrated in Figure 8. For the giant sample, there are two deep blue areas: one is around upper-right corner of the parameter space, and another is around $T_{\text{eff}} = 4900$ K and $\log g = 2.3$. For the main-sequence sample, there is one deep blue area which is around $T_{\text{eff}} = 6200$ K and $\log g = 4.1$. The location of these deep blue areas with minimum $R_{H\alpha}$ values is marked

with a ‘+’ symbol in Figure 8. The distribution of the minimum $R_{H\alpha}$ areas in Figure 8 suggests that, besides the parameter T_{eff} , other stellar atmospheric parameters such as $\log g$ have equal significance in determining the bottom envelope of $R_{H\alpha}$ distribution in the parameter space.

5.3 Distribution of the $R_{H\alpha}$ index in the $T_{\text{eff}} - [\text{Fe}/\text{H}]$ parameter space for the main-sequence and giant samples

Figures 9a and 9b show the distributions of the $R_{H\alpha}$ index values in the $T_{\text{eff}} - [\text{Fe}/\text{H}]$ parameter space for the selected MRS spectra of the main-sequence sample and the giant sample, respectively, with the same $R_{H\alpha}$ color scale as in Figure 7. The data points are stacked in ascending order of their $R_{H\alpha}$ values, with the maximum value at the highest layer and the minimum value at the lowest layer. For comparison with the results in Section 5.1, we also show the scatter plots of $R_{H\alpha}$ versus $[\text{Fe}/\text{H}]$ for the giant sample and the main-sequence sample in Figures 9c and 9d, respectively. The two horizontal lines in Figures 9c and 9d represent $R_{H\alpha} = 1.05 \times 10^{-5}$ and 1.55×10^{-5} , respectively, for distinguishing the three levels of $R_{H\alpha}$ values described in Section 5.2.

It can be seen from Figure 9 that, for the main-sequence sample, the middle-level $R_{H\alpha}$ values (displayed in green) are mainly distributed in a Λ -shaped strip area in the $T_{\text{eff}} - [\text{Fe}/\text{H}]$ space, which swings up and down around $[\text{Fe}/\text{H}] = 0.0$ (solar metallicity) with the vertex at about $T_{\text{eff}} \sim 5400$ K; while for the giant sample, the middle-level $R_{H\alpha}$ values spread over an irregularly shaped area in the $T_{\text{eff}} - [\text{Fe}/\text{H}]$ space, which is distinctly different from that of the main-sequence sample.

Figure 9 also exhibits that the distribution area of the upper-level $R_{H\alpha}$ values (displayed in red) basically coincides with the distribution area of the middle-level $R_{H\alpha}$ values in the $T_{\text{eff}} - [\text{Fe}/\text{H}]$ parameter space for both the main-sequence and giant samples, which results in a spike pattern of the upper-level $R_{H\alpha}$ values in Figure 9d for the main-sequence sample and a fan-shaped pattern of the upper-level $R_{H\alpha}$ values in Figure 9c for the giant sample. The coincidence of the locations of the middle-level and upper-level $R_{H\alpha}$ values in the $T_{\text{eff}} - [\text{Fe}/\text{H}]$ space suggests that they might have the same origin on stars, though corresponding to different levels of activity.

6 Dataset of $H\alpha$ activity indices

The $I_{H\alpha}$ index data and the $R_{H\alpha}$ index data of the LAMOST MRS spectra of F-, G-, and K-type stars analyzed in this work, as well as the related spectroscopic parameters from the LAMOST catalogs, are stored in a CSV-format file (file name: `Halpaha_activity_indices_LAMOST_MRS_DR8.csv`) which is available in the online dataset of this paper. The web link of the dataset is <https://doi.org/10.5281/zenodo.7396963>. The columns included in the dataset are listed and briefly described in Table 1. Some $H\alpha$ indices and spectroscopic parameters are not available for a few of MRS spectra, which are indicated by a value of -9999.0 in the dataset.

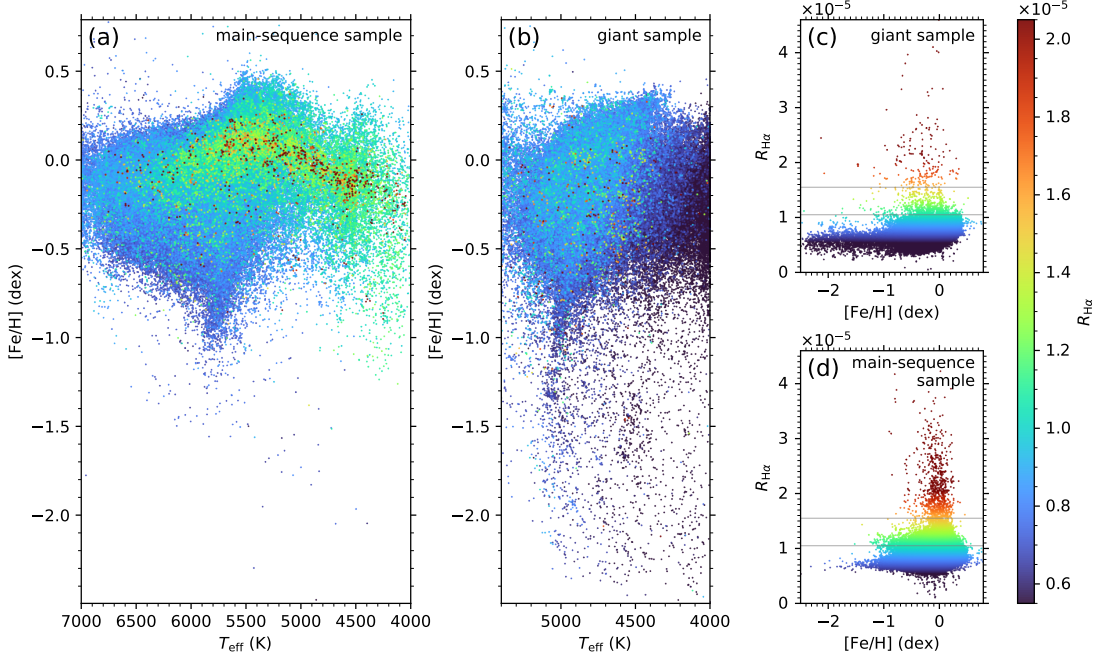


Fig. 9 (a, b) Distributions of the $R_{H\alpha}$ index values in the $T_{\text{eff}} - [Fe/H]$ parameter space for the selected MRS spectra of the main-sequence sample (panel a) and the giant sample (panel b). The value of $R_{H\alpha}$ is indicated by color scale (same as in Figure 7). The data points in the diagrams are stacked in ascending order of their $R_{H\alpha}$ values, with the maximum value at the highest layer and the minimum value at the lowest layer. (c, d) Scatter plots of $R_{H\alpha}$ versus $[Fe/H]$ for the giant sample (panel c) and the main-sequence sample (panel d). Panels c and d use the same $R_{H\alpha}$ color scale as panels a and b. The two horizontal lines in panels c and d represent $R_{H\alpha} = 1.05 \times 10^{-5}$ and 1.55×10^{-5} , respectively, for distinguishing the three levels of $R_{H\alpha}$ values (see main text for details).

7 Conclusion and discussion

In this paper, we investigated the distribution of the stellar $H\alpha$ chromospheric activity with respect to stellar atmospheric parameters (T_{eff} , $\log g$, and $[Fe/H]$) and main-sequence/giant categories for the F-, G-, and K-type stars observed by the LAMOST MRS. A total of 329,294 MRS spectra from LAMOST DR8 were used in the analysis. The $H\alpha$ activity index ($I_{H\alpha}$) and the $H\alpha$ R -index ($R_{H\alpha}$) are evaluated for the MRS spectra. The $H\alpha$ chromospheric activity distributions of the main-sequence and giant samples with respect to individual stellar parameters, as well as in the $T_{\text{eff}} - \log g$ and $T_{\text{eff}} - [Fe/H]$ parameter spaces, were analyzed based on the $R_{H\alpha}$ index.

We have found certain trends of the $R_{H\alpha}$ index distribution with stellar effective temperature (T_{eff}), which are distinctly different for the main-sequence and giant samples. For the main-sequence sample, the distribution has a bowl-shaped lower envelope with a minimum at about 6200 K, a hill-shaped middle envelope with a maximum at about 5600 K, and an upper envelope continuing to increase from hotter to cooler stars; while for the giant sample, the middle and upper envelopes of the

Table 1 Columns included in the dataset of this paper.

Column Name	Unit (if available)	Description
obsid		unique observation identifier of LAMOST MRS
ra	degree	right ascension of the observed object
dec	degree	declination of the observed object
obsdate		UTC date of the observation (format: YYYY-MM-DD)
fitsname		MRS FITS data file name
sn_B		signal-to-noise ratio of the blue band of MRS (S/N_B)
sn_R		signal-to-noise ratio of the red band of MRS (S/N_R)
band_para		indicating which band of MRS is used by the LASP to determine the stellar atmospheric parameters; ‘B’ representing the blue band and ‘R’ representing the red band
teff	K	effective temperature (T_{eff}) determined by the LASP
teff_err	K	uncertainty of T_{eff}
logg	dex	surface gravity ($\log g$) determined by the LASP; g in unit of cm/s^2
logg_err	dex	uncertainty of $\log g$
feh	dex	metallicity ($[\text{Fe}/\text{H}]$) determined by the LASP
feh_err	dex	uncertainty of $[\text{Fe}/\text{H}]$
rv_r0	km/s	radial velocity determined based on the red band data of MRS
rv_r0_err	km/s	uncertainty of rv_r0
category*		‘main-sequence’ or ‘giant’ or ‘intermediate-zone’, as defined in Section 3
I_halpha*		$I_{\text{H}\alpha}$ index, as defined in Section 4.1
I_halpha_err*		uncertainty of $I_{\text{H}\alpha}$
chi*	\AA^{-1}	χ factor, as defined in Section 4.2
chi_err*	\AA^{-1}	uncertainty of χ
R_halpha*		$R_{\text{H}\alpha}$ index, as defined in Section 4.2
R_halpha_err*		uncertainty of $R_{\text{H}\alpha}$

Note: The columns marked with an asterisk are provided by this work. Other columns are from the MRS catalogs of LAMOST DR8 v1.1.

$R_{\text{H}\alpha}$ index distribution first increases with a decrease of T_{eff} and then drop to a lower activity level at about 4300 K. The difference in the $R_{\text{H}\alpha}$ versus T_{eff} distributions of the main-sequence and giant samples reveals the different activity characteristics at different stages of stellar evolution.

The distribution of $R_{\text{H}\alpha}$ with $\log g$ for the main-sequence and giant samples suggests that a larger surface gravity favors a higher $R_{\text{H}\alpha}$ index, but the shape of the envelopes of the $R_{\text{H}\alpha}$ distribution with $\log g$ is complicated and the trend is not monotonic.

Although the morphology of the $R_{\text{H}\alpha}$ index distribution with stellar metallicity ($[\text{Fe}/\text{H}]$) is different for the main-sequence and giant samples, it is found that the upper envelope of the $R_{\text{H}\alpha}$ distribution is higher for stars with $[\text{Fe}/\text{H}]$ greater than about -1.0 , and the metal-poor stars with $[\text{Fe}/\text{H}]$ less than about -1.0 generally have a lower level of $\text{H}\alpha$ activity. This property is the same for both the main-sequence and giant samples. The fact that the lowest-metallicity stars hardly exhibit high $\text{H}\alpha$ indices implies that they might be very old stars.

The distributions of the $R_{\text{H}\alpha}$ index with the three stellar atmospheric parameters for the main-sequence and giant samples exhibit that the $\text{H}\alpha$ chromospheric activity

of giant stars is on average lower than that of main-sequence stars, which is consistent with the results in the literature.

In the $T_{\text{eff}} - \log g$ and $T_{\text{eff}} - [\text{Fe}/\text{H}]$ stellar parameter spaces, it is found that the lower-level $R_{\text{H}\alpha}$ index values ($R_{\text{H}\alpha}$ less than about 1.05×10^{-5}) occupy the largest area of the parameter spaces. The distributions of the middle-level $R_{\text{H}\alpha}$ index values ($R_{\text{H}\alpha}$ between about 1.05×10^{-5} and 1.55×10^{-5}) in the parameter spaces are distinctly different for the main-sequence and giant samples. For the main-sequence sample, the middle-level $R_{\text{H}\alpha}$ values are mainly distributed in the usual main-sequence strip area in the $T_{\text{eff}} - \log g$ parameter space and in a Λ -shaped strip area in the $T_{\text{eff}} - [\text{Fe}/\text{H}]$ parameter space; while for the giant sample, the middle-level $R_{\text{H}\alpha}$ values spread over an irregularly shaped area in the parameter spaces. The distribution area of the upper-level $R_{\text{H}\alpha}$ index values ($R_{\text{H}\alpha}$ greater than about 1.55×10^{-5}) basically coincides with that of the middle-level $R_{\text{H}\alpha}$ values in the $T_{\text{eff}} - [\text{Fe}/\text{H}]$ parameter space, but do not exactly coincide in the $T_{\text{eff}} - \log g$ parameter space, for both the main-sequence and giant samples; this fact suggests that the upper-level and middle-level $R_{\text{H}\alpha}$ values might have the same origin on stars, but are associated with stars at different evolution stages and ages. In general, the younger the star, the higher the activity level.

The minimum values of the $R_{\text{H}\alpha}$ index are around 0.55×10^{-5} for the main-sequence sample and less than about 0.60×10^{-5} for the giant sample. These minimum $R_{\text{H}\alpha}$ index values are distributed in separate areas in the $T_{\text{eff}} - \log g$ parameter space (one area for the main-sequence sample and two areas for the giant sample), suggesting that the stellar atmospheric parameter $\log g$ has equal significance as the parameter T_{eff} in determining the bottom envelope of $R_{\text{H}\alpha}$ distribution in the parameter space.

All the $I_{\text{H}\alpha}$ and $R_{\text{H}\alpha}$ index data obtained in this work are available in the online dataset of this paper. The web link and the data format of the dataset can be found in Section 6.

The $\text{H}\alpha$ chromospheric activity distribution of F-, G-, and K-type stars obtained in this work from the LAMOST MRS data can be cross-compared with the results of the stellar chromospheric activity obtained from the LAMOST LRS data (e.g., Frasca et al 2016; Zhang et al 2020a; Bai et al 2021; Zhang et al 2022), the stellar photospheric activity and flare activity obtained from the light curve data of the *Kepler* and *TESS* missions (e.g., Maehara et al 2012; He et al 2015; Maehara et al 2015; Mehrabi et al 2017; He et al 2018; Goodarzi et al 2019; Günther et al 2020; Goodarzi et al 2021; Okamoto et al 2021; Tu et al 2021; Yan et al 2021), and the stellar coronal activity obtained from the space-based X-ray observations (e.g., Evans et al 2010; Wright et al 2011; Wang et al 2020; Webb et al 2020; Freund et al 2022; Schneider et al 2022). The algorithm and approach developed in this work for the $\text{H}\alpha$ activity indices can be applied to the single-exposure spectra and time-domain data of MRS (e.g., Fu et al 2020; Wang et al 2021; Lu et al 2022; Wu et al 2022b; Han et al 2023), from which the time evolution information of $\text{H}\alpha$ chromosphere activity can be revealed. The dataset provided by this work can also be useful for assessing the impact of stellar activity to the radial velocity signals when searching for exoplanets, as well as when estimating space and atmospheric environment of exoplanets (e.g. Kürster et al 2003; Bonfils et al 2007; Boisse et al 2009; Gomes da Silva et al 2011; Robertson et al 2013, 2016).

Acknowledgements. Guoshoujing Telescope (the Large Sky Area Multi-Object Fiber Spectroscopic Telescope, LAMOST) is a National Major Scientific Project built by the Chinese Academy of Sciences. Funding for the project has been provided by the National Development and Reform Commission. LAMOST is operated and managed by the National Astronomical Observatories, Chinese Academy of Sciences. This work made use of Astropy (Astropy Collaboration et al, 2013, 2018), PyAstronomy (Czesla et al, 2019), PyDL, and SciPy (Virtanen et al, 2020).

Author contributions. The study was carried out in collaboration of all authors. Han He performed the data analysis and wrote the manuscript with input from all coauthors.

Funding. This research is supported by the National Key R&D Program of China (2019YFA0405000) and the National Natural Science Foundation of China (11973059 and 12073001). H.H. acknowledges the CAS Strategic Pioneer Program on Space Science (XDA15052200) and the B-type Strategic Priority Program of the Chinese Academy of Sciences (XDB41000000). W.Z. and J.Z. acknowledge the support of the Anhui Project (Z010118169).

Data Availability. The dataset generated during the current study is available in the online dataset of this paper (see Section 6 for the web link).

Declarations

Informed Consent. Informed consent was obtained from all individual participants included in the study.

Competing interests. The authors declare no competing interests.

Appendix A Distribution of the $[\text{Fe}/\text{H}]$ values in the $T_{\text{eff}} - \log g$ parameter space

In Figure A1, we show the distribution of the $[\text{Fe}/\text{H}]$ values in the $T_{\text{eff}} - \log g$ parameter space for the MRS spectra of F-, G-, and K-type stars analyzed in this work. The values of the stellar atmospheric parameters (T_{eff} , $\log g$, and $[\text{Fe}/\text{H}]$) are provided by the LAMOST Stellar Parameter Pipeline (LASP) and are determined by matching the observed MRS spectra with the reference spectra. Panel a of Figure A1 mainly shows the distribution of the positive $[\text{Fe}/\text{H}]$ values (displayed in red) in the $T_{\text{eff}} - \log g$ parameter space, and panel b mainly shows the distribution of the negative $[\text{Fe}/\text{H}]$ values (displayed in blue). The result exhibited in Figure A1 does not suggest a degeneracy (apparent correlation) between the values of $[\text{Fe}/\text{H}]$ and the values of T_{eff} (or $\log g$) provided by the LASP, demonstrating the reliability of the stellar parameter values.

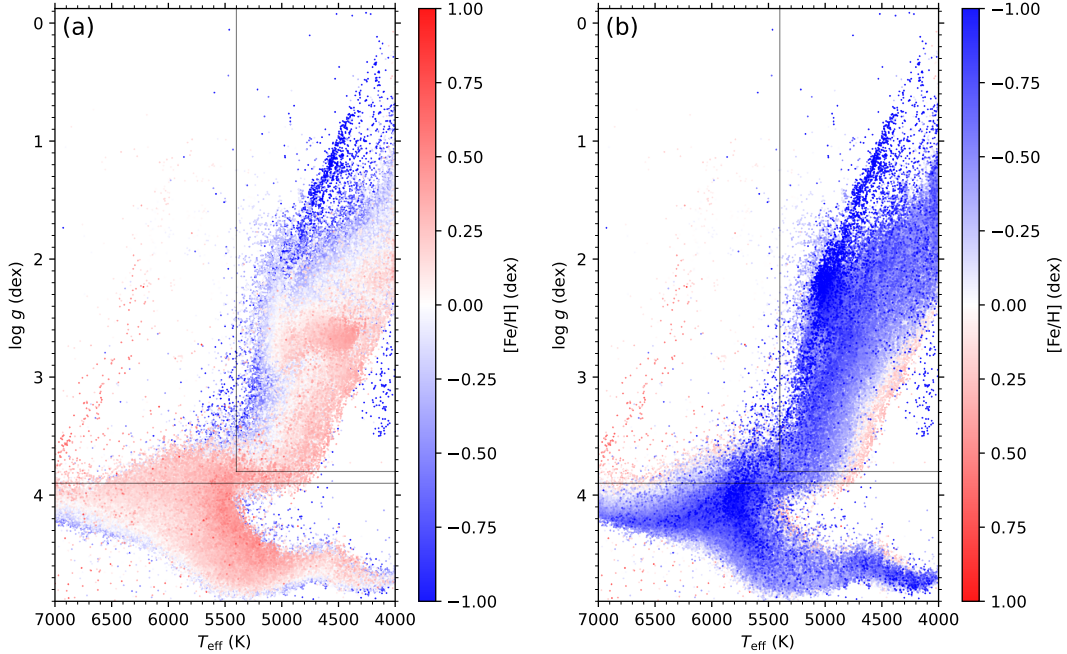


Fig. A1 Distribution of the $[\text{Fe}/\text{H}]$ values in the $T_{\text{eff}} - \log g$ parameter space for the MRS spectra of F-, G-, and K-type stars analyzed in this work. The value of $[\text{Fe}/\text{H}]$ is indicated by color scale (red for positive and blue for negative). In panel a, the data points are stacked in ascending order of their $[\text{Fe}/\text{H}]$ values, with the maximum value at the highest layer and the minimum value at the lowest layer. In panel b, the data points are stacked in reverse order of their $[\text{Fe}/\text{H}]$ values, with the minimum value at the highest layer and the maximum value at the lowest layer. The horizontal and vertical lines in the two panels are the dividing lines for the main-sequence and giant samples (same as in Figure 3).

Appendix B Relationship between the magnitudes of $v \sin i$ and $\Delta I_{\text{H}\alpha}$

We estimate the relationship between the magnitudes of $v \sin i$ (projected rotational velocity) and $\Delta I_{\text{H}\alpha}$ (increment of $I_{\text{H}\alpha}$ caused by rotational broadening) by using the nine example spectra shown in Figure 1. These spectra are from different stellar types and at different $\text{H}\alpha$ activity levels and hence are representative.

For an input spectrum of $\text{H}\alpha$ line and a given $v \sin i$ value, the spectral profile after rotational broadening can be calculated by using the formula given by Gray (2008). For each of the spectra displayed in Figure 1, we calculate a series of spectra after applying rotational broadening for a series of $v \sin i$ values from 0 km/s to 30 km/s,³ and then evaluate $I_{\text{H}\alpha}$ values for each of the calculated spectra. The $\Delta I_{\text{H}\alpha}$ values corresponding to the series of $v \sin i$ values are obtained by subtracting the $I_{\text{H}\alpha}$ value of the original spectrum from the newly evaluated $I_{\text{H}\alpha}$ values. (Note that the value of

³The limb-darkening coefficient ϵ is set to 0.6 in the calculation.

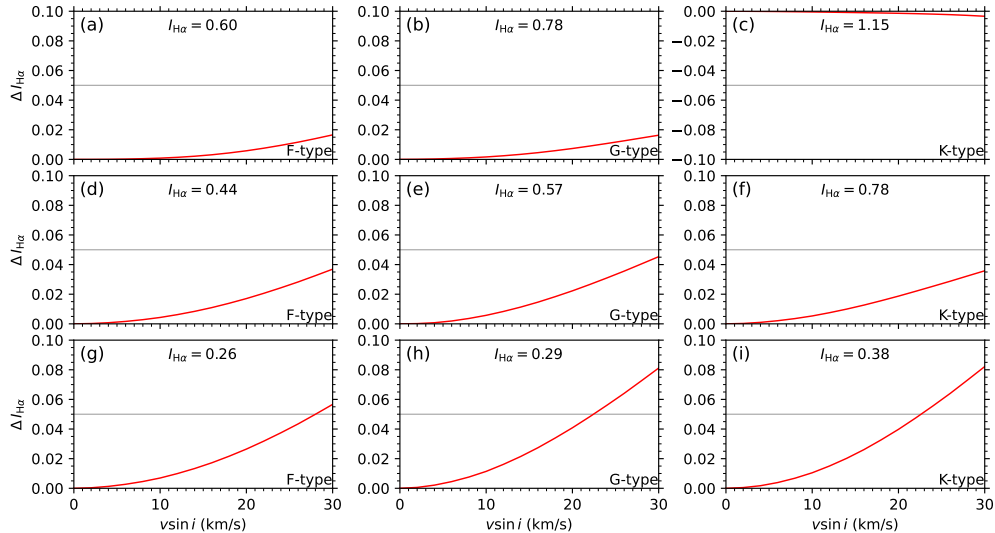


Fig. B2 Plots of $vsini - \Delta I_{H\alpha}$ relation (red curve) for the nine example spectra shown in Figure 1. The horizontal line in the plots represents $|\Delta I_{H\alpha}| = 0.05$. The $I_{H\alpha}$ values of the original spectra (corresponding to $vsini = 0$ km/s in the horizontal axis) are given in the plots. In panel c, $\Delta I_{H\alpha}$ takes a negative value owing to the emission profile of the $H\alpha$ line.

$\Delta I_{H\alpha}$ is positive for the $H\alpha$ absorption line profile and negative for the $H\alpha$ emission line profile.)

The plots of $vsini - \Delta I_{H\alpha}$ relation for all the nine example spectra are shown in Figure B2. It can be seen from Figure B2 that, for $vsini$ values less than 30 km/s, the absolute magnitude of $\Delta I_{H\alpha}$ is generally below about $0.02 \sim 0.05$ for higher $I_{H\alpha}$ values (panels a–f) and below about $0.06 \sim 0.08$ for lower $I_{H\alpha}$ values (panels g–i).

It should be noted that a comparison between the $vsini$ values obtained by the LAMOST MRS and by the Apache Point Observatory Galactic Evolution Experiment (APOGEE; Majewski et al 2017) shows that the $vsini$ by the MRS is slightly larger than that by the APOGEE (see the data release documents of LAMOST for more details), and the original MRS spectra used for analyzing the $vsini - \Delta I_{H\alpha}$ relation might have a small but non-zero intrinsic $vsini$. Therefore, the $vsini - \Delta I_{H\alpha}$ relation and the upper limit of $\Delta I_{H\alpha}$ displayed in Figure B2 can be regarded as an estimate of magnitude rather than a precise result.

Appendix C Algorithm for $\delta\chi$ estimation

The χ factor defined in Equation (6) is a function of stellar atmospheric parameters T_{eff} , $\log g$, and $[\text{Fe}/\text{H}]$, thus the uncertainty of χ (i.e., $\delta\chi$) depends on the uncertainties of the three stellar atmospheric parameters δT_{eff} , $\delta \log g$, and $\delta[\text{Fe}/\text{H}]$.

We use $\delta\chi(T_{\text{eff}})$, $\delta\chi(\log g)$, and $\delta\chi([\text{Fe}/\text{H}])$ to denote the uncertainties of χ caused by the uncertainties of the three stellar atmospheric parameters. To estimate $\delta\chi(T_{\text{eff}})$, we first calculate three χ values corresponding to T_{eff} , $T_{\text{eff}} - \delta T_{\text{eff}}$, and $T_{\text{eff}} + \delta T_{\text{eff}}$,

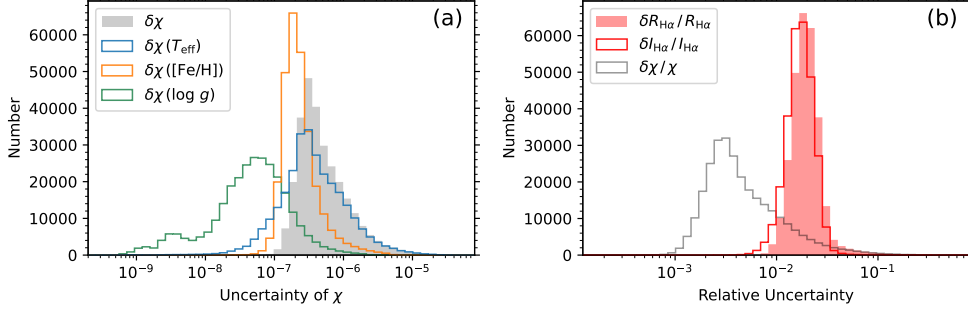


Fig. C3 (a) Histograms of $\delta\chi$, $\delta\chi(T_{\text{eff}})$, $\delta\chi([\text{Fe}/\text{H}])$, and $\delta\chi(\log g)$ for the MRS spectra analyzed in this work. (b) Histograms of $\delta R_{\text{H}\alpha}/R_{\text{H}\alpha}$, $\delta I_{\text{H}\alpha}/I_{\text{H}\alpha}$, and $\delta\chi/\chi$ for the MRS spectra analyzed in this work.

which are denoted by $\chi(T_{\text{eff}})$, $\chi(T_{\text{eff}} - \delta T_{\text{eff}})$, and $\chi(T_{\text{eff}} + \delta T_{\text{eff}})$ respectively. Then, the value of $\delta\chi(T_{\text{eff}})$ is calculated by the following equation:

$$\delta\chi(T_{\text{eff}}) = \frac{|\chi(T_{\text{eff}} - \delta T_{\text{eff}}) - \chi(T_{\text{eff}})| + |\chi(T_{\text{eff}} + \delta T_{\text{eff}}) - \chi(T_{\text{eff}})|}{2}. \quad (\text{C1})$$

$\delta\chi(\log g)$ and $\delta\chi([\text{Fe}/\text{H}])$ can be estimated similarly.

The value of $\delta\chi$ is calculated from the values of $\delta\chi(T_{\text{eff}})$, $\delta\chi(\log g)$, and $\delta\chi([\text{Fe}/\text{H}])$ by the following formula:

$$\delta\chi = \sqrt{[\delta\chi(T_{\text{eff}})]^2 + [\delta\chi(\log g)]^2 + [\delta\chi([\text{Fe}/\text{H}])]^2}. \quad (\text{C2})$$

In Figure C3a, we compare the histograms of $\delta\chi(T_{\text{eff}})$, $\delta\chi(\log g)$, $\delta\chi([\text{Fe}/\text{H}])$, and $\delta\chi$ for the MRS spectra analyzed in this work. It can be seen from Figure C3a that the value of $\delta\chi$ is mainly affected by $\delta\chi(T_{\text{eff}})$, and $\delta\chi(\log g)$ has the least effect on the $\delta\chi$ result.

In Figure C3b, we compare the histograms of the relative uncertainties of χ , $I_{\text{H}\alpha}$, and $R_{\text{H}\alpha}$ (i.e., $\delta\chi/\chi$, $\delta I_{\text{H}\alpha}/I_{\text{H}\alpha}$, and $\delta R_{\text{H}\alpha}/R_{\text{H}\alpha}$) for the MRS spectra analyzed in this work. It can be seen from Figure C3b that the relative uncertainty of $R_{\text{H}\alpha}$ ($\delta R_{\text{H}\alpha}/R_{\text{H}\alpha}$) is mainly affected by $\delta I_{\text{H}\alpha}/I_{\text{H}\alpha}$, and for most MRS spectra $\delta\chi/\chi$ is much smaller than $\delta I_{\text{H}\alpha}/I_{\text{H}\alpha}$. The influence of $\delta\chi/\chi$ on $\delta R_{\text{H}\alpha}/R_{\text{H}\alpha}$ is only prominent for a small number of spectra with relatively large uncertainties of T_{eff} .

References

- Allard F (2016) The PHOENIX Model Atmosphere Grid for Stars. In: Reylé C, Richard J, Cambrésy L, et al (eds) SF2A-2016: Proceedings of the Annual meeting of the French Society of Astronomy and Astrophysics, pp 223–227

- Allard F, Hauschildt PH (1995) Model Atmospheres for M (Sub)Dwarf Stars. I. The Base Model Grid. *Astrophys. J.*445:433. <https://doi.org/10.1086/175708>
- Astropy Collaboration, Robitaille TP, Tollerud EJ, et al (2013) Astropy: A community Python package for astronomy. *Astron. Astrophys.*558:A33. <https://doi.org/10.1051/0004-6361/201322068>
- Astropy Collaboration, Price-Whelan AM, Sipőcz BM, et al (2018) The Astropy Project: Building an Open-science Project and Status of the v2.0 Core Package. *Astron. J.*156:123. <https://doi.org/10.3847/1538-3881/aabc4f>
- Astudillo-Defru N, Delfosse X, Bonfils X, et al (2017) Magnetic activity in the HARPS M dwarf sample. The rotation-activity relationship for very low-mass stars through R'_{HK} . *Astron. Astrophys.*600:A13. <https://doi.org/10.1051/0004-6361/201527078>
- Bai ZR, Zhang HT, Yuan HL, et al (2021) The first data release of LAMOST low-resolution single-epoch spectra. *Research in Astronomy and Astrophysics* 21:249. <https://doi.org/10.1088/1674-4527/21/10/249>
- Baliunas SL, Donahue RA, Soon WH, et al (1995) Chromospheric Variations in Main-Sequence Stars. II. *Astrophys. J.*438:269. <https://doi.org/10.1086/175072>
- Baraffe I, Homeier D, Allard F, et al (2015) New evolutionary models for pre-main sequence and main sequence low-mass stars down to the hydrogen-burning limit. *Astron. Astrophys.*577:A42. <https://doi.org/10.1051/0004-6361/201425481>
- Boisse I, Moutou C, Vidal-Madjar A, et al (2009) Stellar activity of planetary host star HD 189 733. *Astron. Astrophys.*495:959–966. <https://doi.org/10.1051/0004-6361:200810648>
- Bonfils X, Mayor M, Delfosse X, et al (2007) The HARPS search for southern extra-solar planets. X. A $m \sin i = 11M_{\oplus}$ planet around the nearby spotted M dwarf GJ 674. *Astron. Astrophys.*474:293–299. <https://doi.org/10.1051/0004-6361:20077068>
- Buder S, Lind K, Ness MK, et al (2019) The GALAH survey: An abundance, age, and kinematic inventory of the solar neighbourhood made with TGAS. *Astron. Astrophys.*624:A19. <https://doi.org/10.1051/0004-6361/201833218>
- Chen X, Ge Z, Chen Y, et al (2022) Ages of Main-sequence Turnoff Stars from the GALAH Survey. *Astrophys. J.*929:124. <https://doi.org/10.3847/1538-4357/ac55a1>
- Ciddor PE (1996) Refractive index of air: new equations for the visible and near infrared. *Appl. Opt.*35:1566–1573. <https://doi.org/10.1364/AO.35.001566>
- Cui XQ, Zhao YH, Chu YQ, et al (2012) The Large Sky Area Multi-Object Fiber Spectroscopic Telescope (LAMOST). *Research in Astronomy and Astrophysics* 12:1197–1242. <https://doi.org/10.1088/1674-4527/12/9/003>

- Czesla S, Schröter S, Schneider CP, et al (2019) PyA: Python astronomy-related packages. *Astrophysics Source Code Library*, record ascl:1906.010
- Duncan DK, Vaughan AH, Wilson OC, et al (1991) CA II H and K Measurements Made at Mount Wilson Observatory, 1966–1983. *Astrophys. J. Suppl. Ser.*76:383. <https://doi.org/10.1086/191572>
- Evans IN, Primini FA, Glotfelty KJ, et al (2010) The Chandra Source Catalog. *Astrophys. J. Suppl. Ser.*189:37–82. <https://doi.org/10.1088/0067-0049/189/1/37>
- Fang C, Chen PF, Li Z, et al (2013) A new multi-wavelength solar telescope: Optical and Near-infrared Solar Eruption Tracer (ONSET). *Research in Astronomy and Astrophysics* 13:1509–1517. <https://doi.org/10.1088/1674-4527/13/12/011>
- Frasca A, Molenda-Żakowicz J, De Cat P, et al (2016) Activity indicators and stellar parameters of the Kepler targets. An application of the ROTFIT pipeline to LAMOST-Kepler stellar spectra. *Astron. Astrophys.*594:A39. <https://doi.org/10.1051/0004-6361/201628337>
- Frebel A, Norris JE (2015) Near-Field Cosmology with Extremely Metal-Poor Stars. *Annu. Rev. Astron. Astrophys.*53:631–688. <https://doi.org/10.1146/annurev-astro-082214-122423>
- Freund S, Czesla S, Robrade J, et al (2022) The stellar content of the ROSAT all-sky survey. *Astron. Astrophys.*664:A105. <https://doi.org/10.1051/0004-6361/202142573>
- Fu JN, Cat PD, Zong W, et al (2020) Overview of the LAMOST-Kepler project. *Research in Astronomy and Astrophysics* 20:167. <https://doi.org/10.1088/1674-4527/20/10/167>
- García RA, Ballot J (2019) Asteroseismology of solar-type stars. *Living Reviews in Solar Physics* 16:4. <https://doi.org/10.1007/s41116-019-0020-1>
- Gomes da Silva J, Santos NC, Bonfils X, et al (2011) Long-term magnetic activity of a sample of M-dwarf stars from the HARPS program. I. Comparison of activity indices. *Astron. Astrophys.*534:A30. <https://doi.org/10.1051/0004-6361/201116971>
- Goodarzi H, Mehrabi A, Khosroshahi HG, et al (2019) Flare Activity and Magnetic Feature Analysis of the Flare Stars. *Astrophys. J. Suppl. Ser.*244:37. <https://doi.org/10.3847/1538-4365/ab44cd>
- Goodarzi H, Mehrabi A, Khosroshahi HG, et al (2021) Flare Activity and Magnetic Feature Analysis of the Flare Stars. II. Subgiant Branch. *Astrophys. J.*906:40. <https://doi.org/10.3847/1538-4357/abc8ea>
- Gray DF (2008) *The Observation and Analysis of Stellar Photospheres*. Cambridge University Press, Cambridge, UK

- Günther MN, Zhan Z, Seager S, et al (2020) Stellar Flares from the First TESS Data Release: Exploring a New Sample of M Dwarfs. *Astron. J.*159:60. <https://doi.org/10.3847/1538-3881/ab5d3a>
- Hale GE (1929) The Spectroheliograph and its Work. *Astrophys. J.*70:265–311. <https://doi.org/10.1086/143226>
- Hall JC (2008) Stellar Chromospheric Activity. *Living Reviews in Solar Physics* 5:2. <https://doi.org/10.12942/lrsp-2008-2>
- Han H, Wang S, Bai Y, et al (2023) Stellar Chromospheric Activities Revealed from the LAMOST-K2 Time-domain Survey. *Astrophys. J. Suppl. Ser.*264:12. <https://doi.org/10.3847/1538-4365/ac9eac>
- Hartmann L, Soderblom DR, Noyes RW, et al (1984) An analysis of the Vaughan-Preston survey of chromospheric emission. *Astrophys. J.*276:254–265. <https://doi.org/10.1086/161609>
- He H, Wang H, Yun D (2015) Activity Analyses for Solar-type Stars Observed with Kepler. I. Proxies of Magnetic Activity. *Astrophys. J. Suppl. Ser.*221:18. <https://doi.org/10.1088/0067-0049/221/1/18>
- He H, Wang H, Zhang M, et al (2018) Activity Analyses for Solar-type Stars Observed with Kepler. II. Magnetic Feature versus Flare Activity. *Astrophys. J. Suppl. Ser.*236:7. <https://doi.org/10.3847/1538-4365/aab779>
- He H, Zhang H, Wang S, et al (2021) Start-up of a Research Project on Activities of Solar-type Stars Based on the LAMOST Sky Survey. *Research Notes of the American Astronomical Society* 5:6. <https://doi.org/10.3847/2515-5172/abd93b>
- Herbig GH (1985) Chromospheric H alpha emission in F8-G3 dwarfs and its connection with the T Tauri stars. *Astrophys. J.*289:269–278. <https://doi.org/10.1086/162887>
- Husser TO, Wende-von Berg S, Dreizler S, et al (2013) A new extensive library of PHOENIX stellar atmospheres and synthetic spectra. *Astron. Astrophys.*553:A6. <https://doi.org/10.1051/0004-6361/201219058>
- Ichimoto K, Ishii TT, Otsuji K, et al (2017) A New Solar Imaging System for Observing High-Speed Eruptions: Solar Dynamics Doppler Imager (SDDI). *Sol. Phys.*292:63. <https://doi.org/10.1007/s11207-017-1082-7>
- Johnson HL (1966) Astronomical Measurements in the Infrared. *Annu. Rev. Astron. Astrophys.*4:193–206. <https://doi.org/10.1146/annurev.aa.04.090166.001205>
- Kiefer R, Broomhall AM, Ball WH (2019) Seismic Signatures of Stellar Magnetic Activity - What Can We Expect from TESS? *Frontiers in Astronomy and Space Sciences* 6:52. <https://doi.org/10.3389/fspas.2019.00052>

- Kürster M, Endl M, Rouesnel F, et al (2003) The low-level radial velocity variability in Barnard's star (= GJ 699). Secular acceleration, indications for convective redshift, and planet mass limits. *Astron. Astrophys.*403:1077–1087. <https://doi.org/10.1051/0004-6361:20030396>
- Lançon A, Gonneau A, Verro K, et al (2021) A comparison between X-shooter spectra and PHOENIX models across the HR-diagram. *Astron. Astrophys.*649:A97. <https://doi.org/10.1051/0004-6361/202039371>
- Linsky JL (2017) Stellar Model Chromospheres and Spectroscopic Diagnostics. *Annu. Rev. Astron. Astrophys.*55:159–211. <https://doi.org/10.1146/annurev-astro-091916-055327>
- Liu C, Fu J, Shi J, et al (2020) LAMOST Medium-Resolution Spectroscopic Survey (LAMOST-MRS): Scientific goals and survey plan. arXiv e-prints [arXiv:2005.07210](https://arxiv.org/abs/2005.07210) [astro-ph.SR]
- Liu Z, Xu J, Gu BZ, et al (2014) New vacuum solar telescope and observations with high resolution. *Research in Astronomy and Astrophysics* 14:705–718. <https://doi.org/10.1088/1674-4527/14/6/009>
- Lu Hp, Tian H, Zhang Ly, et al (2022) Possible detection of coronal mass ejections on late-type main-sequence stars in LAMOST medium-resolution spectra. *Astron. Astrophys.*663:A140. <https://doi.org/10.1051/0004-6361/202142909>
- Luo AL, Zhao YH, Zhao G, et al (2015) The first data release (DR1) of the LAMOST regular survey. *Research in Astronomy and Astrophysics* 15:1095–1124. <https://doi.org/10.1088/1674-4527/15/8/002>
- Lyra W, Porto de Mello GF (2005) Fine structure of the chromospheric activity in Solar-type stars — The H α line. *Astron. Astrophys.*431:329–338. <https://doi.org/10.1051/0004-6361:20040249>
- Maehara H, Shibayama T, Notsu S, et al (2012) Superflares on solar-type stars. *Nature*485:478–481. <https://doi.org/10.1038/nature11063>
- Maehara H, Shibayama T, Notsu Y, et al (2015) Statistical properties of superflares on solar-type stars based on 1-min cadence data. *Earth, Planets and Space* 67:59. <https://doi.org/10.1186/s40623-015-0217-z>
- Majewski SR, Schiavon RP, Frinchaboy PM, et al (2017) The Apache Point Observatory Galactic Evolution Experiment (APOGEE). *Astron. J.*154:94. <https://doi.org/10.3847/1538-3881/aa784d>
- Mehrabi A, He H, Khosroshahi H (2017) Magnetic Activity Analysis for a Sample of G-type Main Sequence Kepler Targets. *Astrophys. J.*834:207. <https://doi.org/10.3847/1538-4357/834/2/207>

- Middelkoop F (1982) Magnetic structure in cool stars. IV - Rotation and CA II H and K emission of main-sequence stars. *Astron. Astrophys.*107:31–35
- Newton ER, Irwin J, Charbonneau D, et al (2017) The H α Emission of Nearby M Dwarfs and its Relation to Stellar Rotation. *Astrophys. J.*834:85. <https://doi.org/10.3847/1538-4357/834/1/85>
- Noyes RW, Hartmann LW, Baliunas SL, et al (1984) Rotation, convection, and magnetic activity in lower main-sequence stars. *Astrophys. J.*279:763–777. <https://doi.org/10.1086/161945>
- Okamoto S, Notsu Y, Maehara H, et al (2021) Statistical Properties of Superflares on Solar-type Stars: Results Using All of the Kepler Primary Mission Data. *Astrophys. J.*906:72. <https://doi.org/10.3847/1538-4357/abc8f5>
- Pasquini L, Pallavicini R (1991) H-alpha absolute chromospheric fluxes in G and K dwarfs and subgiants. *Astron. Astrophys.*251:199–209
- Pecaut MJ, Mamajek EE (2013) Intrinsic Colors, Temperatures, and Bolometric Corrections of Pre-main-sequence Stars. *Astrophys. J. Suppl. Ser.*208:9. <https://doi.org/10.1088/0067-0049/208/1/9>
- Robertson P, Endl M, Cochran WD, et al (2013) H α Activity of Old M Dwarfs: Stellar Cycles and Mean Activity Levels for 93 Low-mass Stars in the Solar Neighborhood. *Astrophys. J.*764:3. <https://doi.org/10.1088/0004-637X/764/1/3>
- Robertson P, Bender C, Mahadevan S, et al (2016) Proxima Centauri as a Benchmark for Stellar Activity Indicators in the Near-infrared. *Astrophys. J.*832:112. <https://doi.org/10.3847/0004-637X/832/2/112>
- Robinson RD, Cram LE, Giampapa MS (1990) Chromospheric H α and Ca II Lines in Late-Type Stars. *Astrophys. J. Suppl. Ser.*74:891–909. <https://doi.org/10.1086/191525>
- Schneider PC, Freund S, Czesla S, et al (2022) The eROSITA Final Equatorial-Depth Survey (eFEDS). The Stellar Counterparts of eROSITA sources identified by machine learning and Bayesian algorithms. *Astron. Astrophys.*661:A6. <https://doi.org/10.1051/0004-6361/202141133>
- Soderblom DR (2010) The Ages of Stars. *Annu. Rev. Astron. Astrophys.*48:581–629. <https://doi.org/10.1146/annurev-astro-081309-130806>
- Stoughton C, Lupton RH, Bernardi M, et al (2002) Sloan Digital Sky Survey: Early Data Release. *Astron. J.*123:485–548. <https://doi.org/10.1086/324741>
- Straižys V, Kuriliene G (1981) Fundamental Stellar Parameters Derived from the Evolutionary Tracks. *Astrophys. Space Sci.*80:353–368. <https://doi.org/10.1007/BF00652936>

- Tu ZL, Yang M, Wang HF, et al (2021) Superflares, Chromospheric Activities, and Photometric Variabilities of Solar-type Stars from the Second-year Observation of TESS and Spectra of LAMOST. *Astrophys. J. Suppl. Ser.*253:35. <https://doi.org/10.3847/1538-4365/abda3c>
- Vaughan AH, Preston GW, Wilson OC (1978) Flux measurements of Ca II H and K emission. *Publ. Astron. Soc. Pac.*90:267–274. <https://doi.org/10.1086/130324>
- Vernazza JE, Avrett EH, Loeser R (1981) Structure of the solar chromosphere. III. Models of the EUV brightness components of the quiet sun. *Astrophys. J. Suppl. Ser.*45:635–725. <https://doi.org/10.1086/190731>
- Virtanen P, Gommers R, Oliphant TE, et al (2020) SciPy 1.0: fundamental algorithms for scientific computing in Python. *Nature Methods* 17:261–272. <https://doi.org/10.1038/s41592-019-0686-2>
- Walkowicz LM, Hawley SL, West AA (2004) The χ Factor: Determining the Strength of Activity in Low-Mass Dwarfs. *Publ. Astron. Soc. Pac.*116:1105–1110. <https://doi.org/10.1086/426792>
- Wang S, Bai Y, He L, et al (2020) Stellar X-Ray Activity Across the Hertzsprung-Russell Diagram. I. Catalogs. *Astrophys. J.*902:114. <https://doi.org/10.3847/1538-4357/abb66d>
- Wang S, Zhang HT, Bai ZR, et al (2021) LAMOST Time-Domain survey: first results of four K2 plates. *Research in Astronomy and Astrophysics* 21:292. <https://doi.org/10.1088/1674-4527/21/11/292>
- Webb NA, Coriat M, Traulsen I, et al (2020) The XMM-Newton serendipitous survey. IX. The fourth XMM-Newton serendipitous source catalogue. *Astron. Astrophys.*641:A136. <https://doi.org/10.1051/0004-6361/201937353>
- West AA, Morgan DP, Bochanski JJ, et al (2011) The Sloan Digital Sky Survey Data Release 7 Spectroscopic M Dwarf Catalog. I. Data. *Astron. J.*141:97. <https://doi.org/10.1088/0004-6256/141/3/97>
- Wilson OC (1968) Flux Measurements at the Centers of Stellar H- and K-Lines. *Astrophys. J.*153:221–234. <https://doi.org/10.1086/149652>
- Wright NJ, Drake JJ, Mamajek EE, et al (2011) The Stellar-activity-Rotation Relationship and the Evolution of Stellar Dynamos. *Astrophys. J.*743:48. <https://doi.org/10.1088/0004-637X/743/1/48>
- Wu CJ, Wu H, Zhang W, et al (2021) LAMOST Medium-Resolution Spectral Survey of Galactic Nebulae (LAMOST MRS-N): An overview of scientific goals and survey plan. *Research in Astronomy and Astrophysics* 21:96. <https://doi.org/10.1088/1674-4527/21/4/96>

- Wu CJ, Wu H, Zhang W, et al (2022a) The Data Processing of the LAMOST Medium-resolution Spectral Survey of Galactic Nebulae (LAMOST MRS-N Pipeline). *Research in Astronomy and Astrophysics* 22:075015. <https://doi.org/10.1088/1674-4527/ac7387>
- Wu Y, Chen H, Tian H, et al (2022b) Broadening and Redward Asymmetry of H α Line Profiles Observed by LAMOST during a Stellar Flare on an M-type Star. *Astrophys. J.*928:180. <https://doi.org/10.3847/1538-4357/ac5897>
- Yan Y, He H, Li C, et al (2021) Characteristic time of stellar flares on Sun-like stars. *Mon. Not. R. Astron. Soc.*505:L79–L83. <https://doi.org/10.1093/mnras/505/1/79>
- Zhang HQ, Wang DG, Deng YY, et al (2007) Solar Magnetism and the Activity Telescope at HSOS. *Chinese J. Astron. Astrophys.*7:281–288. <https://doi.org/10.1088/1009-9271/7/2/12>
- Zhang J, Bi S, Li Y, et al (2020a) Magnetic Activity of F-, G-, and K-type Stars in the LAMOST-Kepler Field. *Astrophys. J. Suppl. Ser.*247:9. <https://doi.org/10.3847/1538-4365/ab6165>
- Zhang LY, Long L, Shi J, et al (2020b) Magnetic activity based on LAMOST medium-resolution spectra and the Kepler survey. *Mon. Not. R. Astron. Soc.*495:1252–1270. <https://doi.org/10.1093/mnras/505/1/1252>
- Zhang LY, Meng G, Long L, et al (2021) Chromospheric Activity of M Stars Based on LAMOST Low- and Medium-resolution Spectral Surveys. *Astrophys. J. Suppl. Ser.*253:19. <https://doi.org/10.3847/1538-4365/abd7a8>
- Zhang W, Zhang J, He H, et al (2022) Stellar Chromospheric Activity Database of Solar-like Stars Based on the LAMOST Low-Resolution Spectroscopic Survey. *Astrophys. J. Suppl. Ser.*263:12. <https://doi.org/10.3847/1538-4365/ac9406>
- Zhao G, Zhao YH, Chu YQ, et al (2012) LAMOST spectral survey — An overview. *Research in Astronomy and Astrophysics* 12:723–734. <https://doi.org/10.1088/1674-4527/12/7/002>